Numerical analysis and optimization of the performance of CO2-Plume Geothermal (CPG) production wells and implications for electric power generation

Author(s):
Ezekiel, Justin; Adams, Benjamin; Saar, Martin O.; Ebigbo, Anozie

Publication date:
2022-01

Permanent link:
https://doi.org/10.3929/ethz-b-000517297

Originally published in:
Geothermics 98, https://doi.org/10.1016/j.geothermics.2021.102270

Geothermics 98 (2022) 102270

Contents lists available at ScienceDirect

Geothermics

journal homepage: www.elsevier.com/locate/geothermics

Numerical analysis and optimization of the performance of CO_2-Plume Geothermal (CPG) production wells and implications for electric power generation

Justin Ezekiel [a,*], Benjamin M. Adams [a], Martin O. Saar [a,b], Anozie Ebigbo [a,c]

[a] Department of Earth Sciences, Geothermal Energy and Geofluids Group, ETH Zurich, Sonneggstrasse 5, 8092 Zurich, Switzerland
[b] Department of Earth and Environmental Sciences, University of Minnesota, 116 Church Street SE, Minneapolis, MN 55455, United States
[c] Hydromechanics Group, Helmut Schmidt University, Holstenhofweg 85, 22043 Hamburg, Germany

ARTICLE INFO

Keywords:
CO_2-plume geothermal
Production well
Wellbore flow regimes
Numerical modeling
Power generation
CO_2 capture utilization and storage (CCUS)

ABSTRACT

CO_2-Plume Geothermal (CPG) power plants can produce heat and/or electric power. One of the most important parameters for the design of a CPG system is the CO_2 mass flowrate. Firstly, the flowrate determines the power generated. Secondly, the flowrate has a significant effect on the fluid pressure drawdown in the geologic reservoir at the production well inlet. This pressure drawdown is important because it can lead to water flow in the reservoir towards and into the borehole. Thirdly, the CO_2 flowrate directly affects the two-phase (CO_2 and water) flow regime within the production well. An annular flow regime, dominated by the flow of the CO_2 phase in the well, is favorable to increase CPG efficiency. Thus, flowrate optimizations of CPG systems need to honor all of the above processes. We investigate the effects of various operational parameters (maximum flowrate, admissible reservoir-pressure drawdown, borehole diameter) and reservoir parameters (permeability anisotropy and relative permeability curves) on the CO_2 and water flow regime in the production well and on the power generation of a CPG system. We use a numerical modeling approach that couples the reservoir processes with the well and power plant systems. Our results show that water accumulation in the CPG vertical production well can occur. However, with proper CPG system design, it is possible to prevent such water accumulation in the production well and to maximize CPG electric power output.

1. Introduction

In the current era of global energy transition to clean and sustainable energy and to address the challenges posed by global climate change, carbon dioxide (CO_2) capture and storage (CCS) in deep saline aquifers and depleted oil and gas reservoirs is widely considered a significant means to reduce CO_2 emissions to the atmosphere (e.g. IPCC, 2005, 2014). One of the promising technologies that supports shifting the world's energy generation to renewables, in this case geothermal energy, while at the same time enabling the safe removal and storage of captured CO_2 in the subsurface, is the concept of CO_2-Plume Geothermal (CPG) power generation, introduced by Randolph and Saar (2011).

CPG involves the injection of (supercritical) CO_2 from an emitter into existing, naturally porous and permeable geologic formations for geothermal energy recovery and eventually permanent geologic storage of the originally injected CO_2, constituting a CO_2 capture, utilization and storage (CCUS) technology. The naturally porous and permeable formations required for CPG are common throughout the world and are seen to exist where economically favorable storage sites have been identified (IPCC, 2005; Coleman Jr. and Cahan, 2012; Procesi et al., 2013; Eccles and Pratson, 2014).

During the CPG approach, the subsurface-injected CO_2 is geothermally heated as it flows through the reservoir. Some of the heated CO_2 is produced back to the land surface and can be used for direct heat utilization and/or electric power generation in a direct CPG turbomachinery power plant (Adams et al., 2015; Ezekiel et al., 2020; 2021). Thereafter, the CO_2 is cooled, any water removed, and the dry CO_2 reinjected into the CO_2 storage reservoir. The general CPG system design, and its variations, have been discussed in detail in multiple publications since Randolph and Saar (2011), including in Adams et al. (2014, 2015, 2021b), Ezekiel et al. (2020, 2021), and Garapati et al. (2015, 2020). Using CO_2 as the subsurface working fluid to extract

* Corresponding author.
E-mail address: chima.ezekiel@kaust.edu.sa (J. Ezekiel).

https://doi.org/10.1016/j.geothermics.2021.102270
Received 5 July 2020; Received in revised form 5 October 2021; Accepted 6 October 2021
Available online 17 October 2021

energy has several advantages over traditional water or brine. Under the conditions of interest, supercritical CO_2 ($scCO_2$) has a much lower kinematic viscosity than water or brine. As a result, CO_2 mass flowrates, and thus advective energy extraction rates, through the reservoir are accordingly higher than those when subsurface water or brine are employed for geothermal energy extraction, all else (e.g. injection-to-production-well fluid pressure gradient as well as reservoir depth, temperature, transmissivity) being equal (Randolph and Saar, 2011; Garapati et al., 2015; Adams et al., 2015; 2021b; Fleming et al., 2020). This kinematic viscosity effect is the main reason for the approximate doubling of electricity generation for CPG under typical (base-case) conditions, compared to hydrothermal electricity generation, as shown for example by Randolph and Saar (2011) and Adams et al. (2015). Additionally, the higher thermal expansivity of $scCO_2$, compared to liquid water or brine, results in a so-called thermosiphon effect that reduces or eliminates parasitic pumping power requirements (Atrens et al., 2009; Adams et al., 2014).

Previous CPG analyses (Randolph and Saar, 2011; Garapati et al., 2015; Adams et al., 2014, 2015, 2021b) as well as CO_2-based Enhanced Geothermal System (EGS) studies (Brown, 2000; Pruess, 2008, 2006; Atrens et al., 2009) focused on subsurface heat transfer or surface components of the system without accounting for the effect of liquid water entering the production well on CO_2 production and circulation. The pre-test modeling of the first field-scale experiment of a CO_2-thermosiphon (to test the concept of supercritical CO_2 heat extraction from the subsurface) conducted at the South Eastern Regional Partnership for Carbon Sequestration (SECARB) Cranfield Site (Mississippi, USA) initially predicted a sustainable thermosiphon should be possible at the site. However, this particular field test showed that its thermosiphon (initiated by venting the production well) decayed quickly and could not be sustained (Freifeld et al., 2016; Pan et al., 2015, 2018). They postulated that liquid water entering the production well could be one of the important factors damping the CO_2 thermosiphon flowrate.

Most gas production wells have liquid (water) entering the well. If the gas velocities are not high enough, the water accumulates, forming slugs. Such slug formation may cause the overall fluid density to increase in the production well. The higher density increases the bulk weight of fluids in the production well, resulting in decreased flow (velocity) for a given pressure gradient. This transient process, called liquid loading, continues until the well is filled with water. To remove the liquid water in a gas production well, the oil and gas industries apply artificial lift and/or pumping (Lea et al., 2008). Also, they usually use small-diameter production pipes for gas production, which reduces the probability of slug or churn flow in the production well. In contrast, for conventional geothermal energy extraction (using water as the subsurface working fluid), large-diameter production wells are preferred in order to ensure large mass flowrates and minimize heat loss. In CPG systems, brine and CO_2 are typically present in the partially CO_2-saturated reservoir around the injection and production well regions with varying ratios of water–CO_2 saturation. As such, the produced fluid may contain a mixture of water and CO_2. However, large amounts of water in the CPG production well can be detrimental to the performance of the well and the CPG power plant, which may ultimately reduce the efficiency of the CO_2-based geothermal energy system (Freifeld et al., 2016; Pan et al., 2018).

Water influx into the production well, added to any water that exothermally exsolves (increasing the power generation of CPG systems) from the CO_2 as the CO_2 rises in the production well (Fleming et al., 2020), also poses a problem because the produced water must be removed before CO_2 reinjection into the reservoir (Garapati et al., 2015). The removed water must then be disposed of at the land surface or reinjected elsewhere, which, among other concerns, may significantly reduce the CO_2 mass flowrate. Therefore, for successful CPG deployment, it is important to investigate the optimal fluid pressure drawdown, fluid flowrate, and production well pipe diameter to:

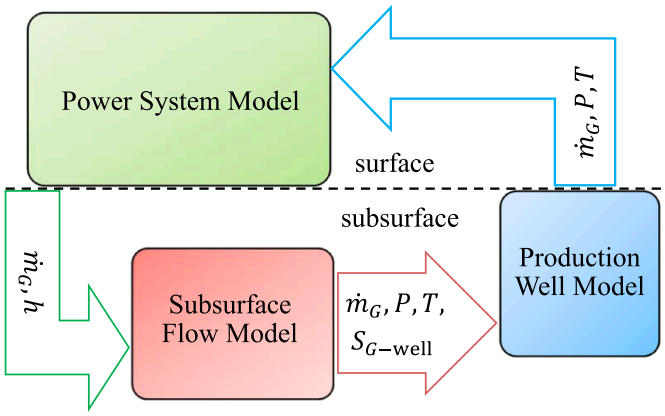

Fig. 1. Numerical modeling concept. The boxes represent separate models, while the arrows represent the information that is passed between the models (pressure, P [Pa], temperature, T [°C], volume fraction of CO_2 in the borehole, S_{G-well} [-], CO_2 mass flowrate, $\dot{m}_G$ [kg/s], and CO_2 specific enthalpy, h [J/kg]). The injection well is not modeled.

a) Reduce the tendency of liquid water to enter the production well,
b) Avoid slug/churn flow and liquid loading in the production well, and
c) Minimize heat and pressure losses as the fluid moves up to the wellhead.

The CO_2 flowrate in the production well is an important factor in the above, as it determines:

a) How much liquid water is drawn into the production well, i.e. water upconing.
b) Whether the water entering the well can accumulate in the well, and
c) How large the achievable power output is.

In prior CPG studies, the production mass flowrate has either been chosen arbitrarily (e.g. Garapati et al., 2015; Randolph and Saar, 2011) or has been based on a power-flowrate analysis to maximize net power generation (e.g. Adams et al., 2015, 2021b). The most important parameters for such an analysis include reservoir depth, temperature, permeability, and thickness as well as well diameter and well spacing (Adams et al., 2021b). However, minimizing the amount of liquid water in the production well is an additional constraint that likely requires consideration when determining optimal CO_2 circulation flowrates of CPG systems.

Hence, the objective of this study is to investigate the fluid flow performance of the CPG production well for different reservoir and CPG operational conditions. In that regard, we employ a coupled flow (reservoir and production well) and power generation model to determine possible factors that may influence the flow regimes and potential water accumulation rates in the CPG production well, and the power generation performance of CPG systems. We also present insights into the failure of the Cranfield (Mississippi, USA) CO_2 thermosiphon field test, conducted in January 2015, due to liquid water occurrence in the production well.

2. Numerical modeling concept

The Introduction section includes references to various CPG system designs. Here, the CPG system is simulated employing several numerical models coupled sequentially to each other by passing relevant model output from one component to the next, as shown in Fig. 1. The subsurface flow model describes the two-phase flow of CO_2 and brine in the reservoir. The production well model determines how the conditions in the well change as the fluid moves upwards. The power-system model calculates the electric power output. In the following sections, each

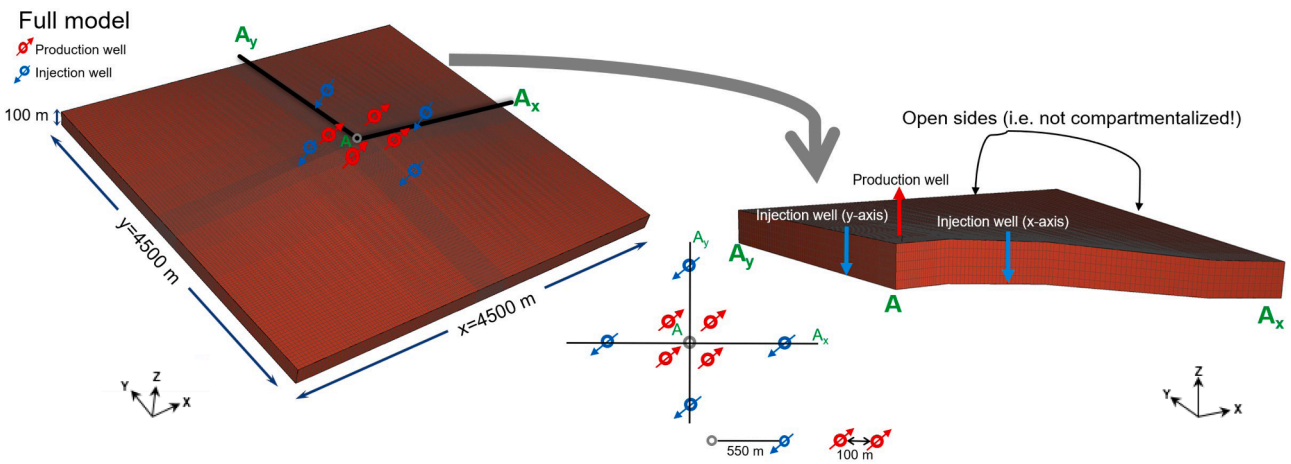

Fig. 2. The full model (left) and the symmetric quarter model (right), showing the location of the production and injection wells. Note that the overlying, impermeable caprock is not shown. The lateral sides of the model are open (i.e. the reservoir is not compartmentalized). The injection (blue) to production (red) well distance is 500 m.

Table 1
Parameters for the base case reservoir model.

Parameter	Value
Reservoir size [km x km x km]	4.5 × 4.5 × 0.1
Depth [km]	2.5
Porosity [-]	0.20
Horizontal permeability, k_h [m^2]	10^{-13} (100 mD)
Thickness [m]	100
Reservoir initial pressure [Pa]	Hydrostatic (25 MPa at the top of the reservoir)
Reservoir initial temperature [°C]	100
Initial CO_2 mass fraction	0.025 (dissolved in brine)
Residual CO_2 saturation [-]	0.10
Residual brine saturation [-]	0.25
van Genuchten parameters α [Pa], m [-]	3×10^3, 0.77
Native brine NaCl saturation [ppm]	150,000
Molecular diffusivity in gas; in liquid water [m^2/s]	10^{-5}; 10^{-10}
Rock grain density [kg/m^3]	2650
Thermal conductivity λ_{wet}, λ_{dry} [W/(m °C)] *	2.51, 1.6
Rock specific heat capacity [J/(kg °C)]	1000
Geothermal gradient [°C/km]	37
Rock compressibility [1/Pa]	10^{-10}
CO_2 injection specific enthalpy [J/kg] **	2.4×10^5
Injection-production well distance [m]	~500
Lateral boundary conditions of the reservoir	Hydrostatic pressure; 100 °C (Dirichlet boundary conditions).
Top and bottom boundary conditions of the reservoir	No fluid flow and no heat flux.
Initial conditions	Hydrostatic equilibrium, no heat flow, pore space entirely occupied by brine.

* λ_{wet} and λ_{dry} are formation heat conductivity under fully water-saturated and fully gas-saturated conditions, respectively. Here, Somerton's interpolation formula for heat conductivity, λ, as a function of water saturation, S_L, is used, i.e. $\lambda(S_L) = \lambda_{dry} + (S_L^{0.5}[\lambda_{wet} - \lambda_{dry}])$ (Somerton, 1992).
** Estimated given the average pressure and temperature of CO_2 at the injection wellhead, determined from the power plant model in Section 2.3.

model and the interfaces between the models are described.

2.1. Subsurface flow model

We set up a generic three-dimensional, homogeneous, axisymmetric geothermal reservoir model comprising a brine-saturated aquifer formation with an anticlinal structure (Fig. 2). The model's geometry and well configuration is similar to the one used in a previous study (Ezekiel et al., 2020). The aquifer formation is bounded by impermeable bedrock and caprock formations. The properties of the geothermal reservoir model are given in Table 1. This reservoir model serves as an initial, conceptual, small-scale system having only four production wells.

The numerical reservoir simulator employed in this study is TOUGH2 (Pruess et al., 2012) with the fluid property module "ECO2N" to provide fluid properties for water and CO_2 (Pruess and Spycher, 2007). The pressure at the bottom of the well (screened interval), which is a function of the wellbore flowrate, is determined using the Thiem approximation (Coats, 1977; Pruess et al., 2012).

In this study, the numerical simulation consists of two stages. The first stage is called the CO_2 plume establishment (PE) stage. During this first stage, CO_2 is injected into the reservoir, displaces brine and develops the CO_2 plume. This stage is crucial since a sufficient amount of CO_2 in the reservoir is necessary to minimize water upconing at the production well once production commences. During the PE stage, the production wells are shut in and CO_2 is injected at a fixed rate of 30 kg/s/well. This value is chosen to coincide with the CO_2 production rate during the CPG stage (described in the next paragraph). For the base-case model, the PE stage is complete when the CO_2 plume at the production-well region has achieved a pore-space CO_2 saturation of 55.0%.

Once the CO_2 saturation around the production well reaches 55.0%, the CPG stage begins. During this stage, the production wells are open, and a maximum fluid extraction rate at the production well is set. However, the pressure decrease at the production well downhole element due to fluid production is not allowed to surpass 7 MPa. This results in flowrates that are initially low, but gradually increase over several years until the maximum is attained. To determine the flowrate to set, we use a simplified power-to-mass-flowrate model (Adams et al., 2015), described in the Appendix section. The chosen base-case flowrate of 120 kg/s (i.e. 30 kg/s/well) is close to the optimum in terms of power (see Fig. A1). This value will be varied in Section 3.3.1. For this study, the simulation of the CPG stage is set to run for about 40 years in total, which is within the lifespan of power plants. At the land surface, the geothermally heated CO_2 (and possibly some water/brine if not yet removed) is run through a turbine to generate electric power. Thereafter, the CO_2 is cooled/condensed and reinjected into the original reservoir. Any produced water/brine is removed, using a water-CO_2 separator, before the cooled CO_2 is reinjected into the reservoir. The question of disposing of the separated brine, whether at the land surface

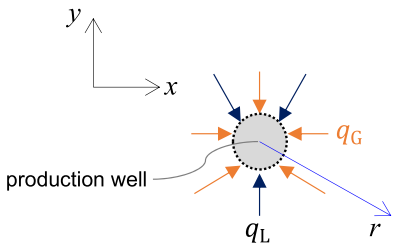

Fig. 3. Top view of the reservoir– well interface. The fluxes of liquid water, q_L, and supercritical/gaseous CO_2, q_G, into the well depend on the mobility of each phase, the horizontal reservoir permeability and the fluid pressure gradient.

or in a different subsurface location, may not be trivial.

2.2. The production wellbore model

2.2.1. Influx of fluids into the borehole

Most gas production wells produce at least some liquid water. When liquid water enters the well with the flowing gas, the gas can carry the water up the well if the velocity of the gas is high enough. If the gas velocity is below the critical minimum velocity required to drag the water droplets out of the production well, then water will accumulate in the production well and liquid loading may eventually occur, which may reduce the productivity and the lifetime of the well. Liquid loading will also increase the pressure drop in the wellbore due to hydrostatic pressure contributions of the flowing fluids (weight of the gas and the accumulated liquid in the wellbore).

In order to assess the relative amounts of free-phase supercritical CO_2, acting essentially like a gas, versus free-phase liquid water entering the inlet of the production well, consider Fig. 3, which shows the top view of the screened interval of the production well. From Darcy's law, there is a fluid flux, q_α [m/s], of Phase α from the reservoir into the borehole due to the radial fluid pressure gradient near the borehole. If one neglects capillary pressure, i.e. assumes $P_L \approx P_G$, then the relative liquid water flux into the well can be approximated by

$$\frac{q_L}{q_L + q_G} \approx \frac{\lambda_L}{\lambda_L + \lambda_G}, \tag{1}$$

where the mobility of Phase α is given by $\lambda_\alpha = \frac{k_{r\alpha}}{\mu_\alpha}$. Here, $k_{r\alpha}$ and μ_α are relative permeability [-] and dynamic viscosity [Pa·s] of Phase α, respectively. Phase α can either be liquid water (L) or supercritical/gaseous CO_2 (G). Note that this assumption may lead to inaccuracies for low liquid water saturations in the reservoir.

Given the relative fluxes into the well, one can estimate the volume fraction of liquid water, S_{L-well}, and the volume fraction of supercritical CO_2, S_{G-well}, at the bottom of the production well,

$$S_{L-well} = \frac{q_L}{q_L + q_G}, \tag{2}$$

$$S_{L-well} \approx \frac{\lambda_L}{\lambda_L + \lambda_G} \text{ and } S_{G-well} \approx \frac{\lambda_G}{\lambda_L + \lambda_G}. \tag{3}$$

As shown in Eq. (1), the mobilities of the phases, and consequently $S_{\alpha-well}$, depend on the relative permeabilities and the viscosities of the phases. The relative permeabilities are functions of the phase saturations in the reservoir rock surrounding the well. The corresponding mass fractions, M_α, defined as the ratio of the mass flowrate of each phase, $\dot{m}_\alpha$ [kg/s], entering the well to the total mass flowrate, $\dot{m}$ [kg/s], are

$$M_L = \frac{S_{L-well} \cdot \varrho_L}{S_{L-well} \cdot \varrho_L + S_{G-well} \cdot \varrho_G} \tag{4}$$

and

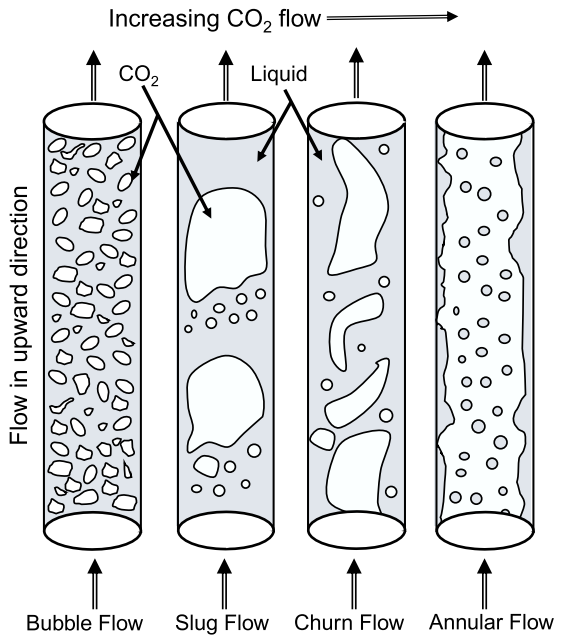

Fig. 4. Two-phase (gas, approximated by supercritical/gaseous CO_2, and liquid, represented by water or brine here) flow regimes in a vertical production well (modified from Yadigaroglu et al., 2018).

$$M_G = \frac{S_{G-well} \cdot \varrho_G}{S_{L-well} \cdot \varrho_L + S_{G-well} \cdot \varrho_G}, \tag{5}$$

where ϱ_L *and* ϱ_G are the densities [kg/m^3] of the liquid and gas phases, respectively. For the evaluation of flow conditions in the borehole, the superficial velocities of the fluid phases, $U_{S,\alpha}$ [m/s], are required. These can be calculated from the information regarding the fluid influx into the well,

$$U_{S,\alpha} = \frac{Q_\alpha}{A} = \frac{\dot{m}_\alpha}{\varrho_\alpha A}, \tag{6}$$

where Q_α [m^3/s] is the volumetric flowrate of Phase α and A [m^2] is the cross-sectional area.

2.2.2. Determining the two-phase flow regimes in the production well

The two-phase (CO_2 and water) flow regime in a vertical CPG production well is determined by the velocity and the relative amounts of the fluid phases in the production well. The four basic flow regimes in a vertical well are – in order of decreasing water content – bubble, slug, churn, and annular flow, as depicted in Fig. 4. For a CPG production well, annular flow is the desired flow regime since it means that the volume fraction of CO_2 in the production well is high and the pressure gradient in the production well is relatively low. Annular flow is important for the density-driven thermosiphon effect because it favors the production of predominantly less-dense CO_2 over water at the land surface, compared to the other flow regimes, associated with a larger water component (thus high density of the produced fluid) at the production wellhead. Annular flow occurs at high gas flowrates. The gas flows upwards in the center of the well as a continuous phase, and any liquid in the well is carried upwards, entrained in the gas as liquid droplets or a mist. If the gas flowrate is not high enough, the droplets fall, accumulate at the bottom of the well, and the flow regime transitions to a slug/churn flow pattern.

We adopt the models of Taitel et al. (1980) for determining the steady-state two-phase upward flow regimes in vertical pipes for our CO_2–water system of fluids. Tatei's model gives distinctive flow-pattern transitions for the four flow regimes that can exist in a vertical pipe.

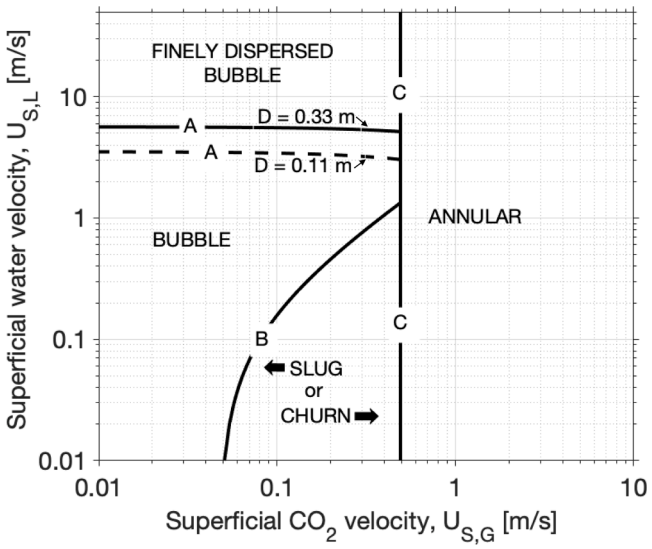

Fig. 5. Flow pattern regimes for vertical production well examples with 0.11 m and 0.33 m pipe diameters, D_w, for the fluid (brine and CO_2) properties, given by our base-case reservoir conditions of 100 °C, 25 MPa, and 0.15 salinity. Note that only the transition boundary between "finely dispersed bubbles" to "bubbles" depends on the production well pipe diameter.

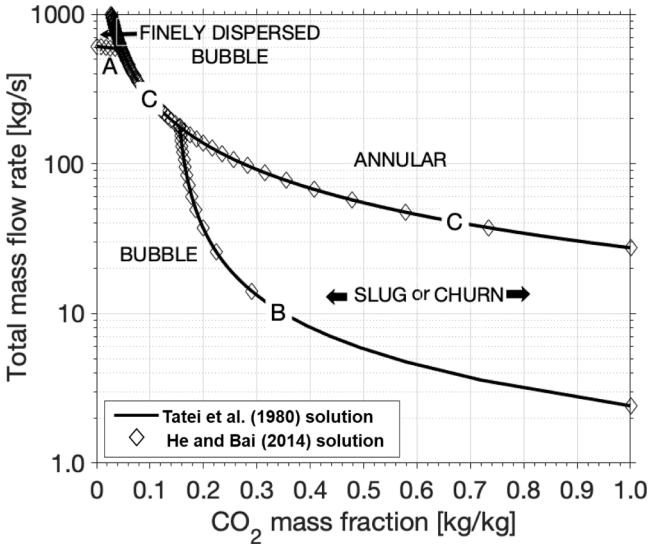

Fig. 6. Flow pattern regimes, denoted by total mass flowrate (of CO_2 and brine with 0.15 salinity) and the mass fraction of CO_2 under our base-case conditions of 100 °C and 25 MPa, with a production well pipe diameter of 0.33 m.

These depend on the flowrates, the fluid properties, and the cross-sectional area of the well. We plot the transition boundaries between three basic CO_2-water flow regimes in Fig. 5.

Fig. 6 is a semi-log plot of total mass flowrate against the CO_2 mass fraction. The figure shows the flow-pattern transitions for this study's base-case fluid properties and a relatively large well pipe diameter of 0.33 m as an example. The calculations are carried out using the conditions near the inlet of the production well. We consider this to be the area with the highest amount of water by volume because, as the fluids rise in the well, the fluid pressure decreases, leading to a significantly greater expansion of the supercritical/gaseous CO_2 than the liquid water and hence a reduction of the volume fraction of water. Hence, we expect the bottom of the well to have the highest volume fraction of free-phase liquid water that originally entered through the well screen. Exsolution of water from CO_2 can take place during the ascent of CO_2, that

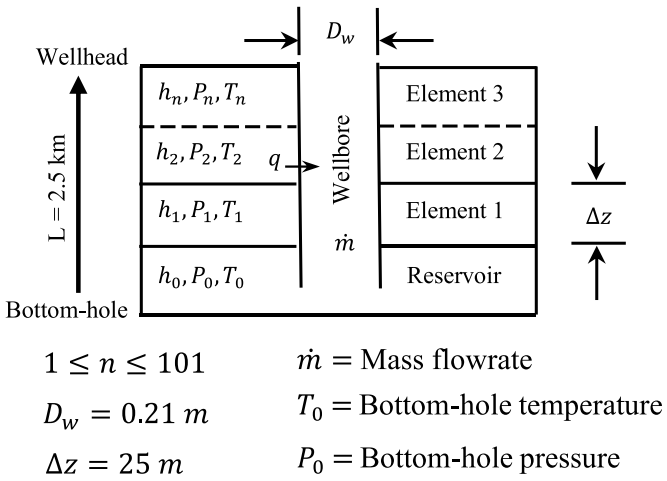

Fig. 7. Schematic of the one-dimensional well model (not to scale), where h, P, and T are the enthalpy, pressure, and temperature, respectively, at each of the 25m-long elements, and q is the heat transfer function of the wellbore model.

originally contained dissolved water, towards the production wellhead (Fleming et al., 2020). However, we ignore this likely minor addition of exsolved, free-phase liquid water here.

In Fig. 6, the solid curves are results obtained by using the flow pattern transition equations from Taitel et al. (1980), while the diamond points are the results obtained by using the equations from He and Bai (2014). The interfacial tension between CO_2 and brine is calculated to be approximately 0.033 N/m (Bachu and Bennion, 2009). The transition curves change significantly with the well pipe diameter. The smaller the well pipe diameter, the lower the minimum flowrate required to achieve annular flow. When the pipe diameter is reduced from 0.33 m (Fig. 6) to 0.11 m, the minimum CO_2 flowrate, required to achieve annular flow, significantly decreases from 25 kg/s to 3 kg/s.

2.2.3. *Flow and heat transport in the production well*

In this study, we implement a simple one-dimensional vertical wellbore model to determine the final temperature and pressure of the produced fluid at the production wellhead. The bottom-hole boundary conditions are defined as the reservoir pressure, temperature, total mass flowrate of the fluid at any given time during fluid production. These are the input values for the wellbore model calculation, as presented in Fig. 1. Brine property values are determined from the relationships provided by Haas (1976) and Phillips et al. (1981) for density and viscosity calculations, respectively.

We set up a vertical production well (2500 m long), which is divided into 100 equal elements Fig. 7). We develop the model in MATLAB using the CoolProp-MATLAB wrapper (Bell et al., 2014) for the iterative calculation of the thermodynamic properties of the fluid components, using the standard equations of state (Bell et al., 2014; Bell and Jäger, 2016). We implement the methodology of Adams et al. (2015) to numerically calculate the fluid state in the production well across each 25m-long vertical well element, Δz, as the fluid flows up inside the well as shown in Fig. 7. This is based on energy, mass – Eqs. (7) and (8) – and momentum conservation equations with which the superficial velocity and temperature of CO_2 are determined in the next-higher wellbore element,

$$h_i + \frac{U_{S,G,i}^2}{2} + g z_i = h_{i-1} + \frac{U_{S,G,i-1}^2}{2} + g z_{i-1} - \left[(\pi \Delta z D_w) q \Big/ \dot{m}_G \right], \tag{7}$$

$$\dot{m}_G = \varrho_{G,i-1}\, A\, U_{S,G,i-1} = \varrho_{G,i}\, A\, U_{S,G,i}. \tag{8}$$

The subscript i denotes the element number, running from bottomhole to wellhead, g is gravitational acceleration, and q is the heat flux be-

Table 2
Parameters for the wellbore and power plant models.

Parameters	Base case values
Well length [m]	2500
Well pipe diameter [m]	0.21
Wellbore flowing bottom-hole pressure [MPa]*	18
Productivity index [(m^3]**	3.89×10^{-12}
Fluid components	CO_2 and Brine
Mean formation thermal conductivity [W/(m °C)]	2.51
Mean formation density [kg/m^3]	2650
Mean formation specific heat capacity [J/(kg °C)]	1000
Well pipe material and surface roughness [m]	Bare CR13; 55×10^{-6} (Adams et al., 2015; Farshad and Rieke, 2006)
Power system	Direct CO_2 system – no pumping requirement
Direct turbine isentropic efficiency	0.78
Mean annual ambient air temperature [°C]	8 7
Condensing or cooling tower approach temperature [°C]	
CO_2 injection temperature at the surface [°C]	15

* The wellbore flowing bottom-hole pressure, P_{wb}, is fixed at 18 MPa (for the base case) and the flowrate increases according to the set productivity index. At the maximum flowrate (fixed at 30 kg/s/well for the base case), P_{wb} varies and is calculated by $\dot{m}_G = \frac{k_{rG}}{\mu_G}\rho_G \cdot PI \cdot (P_G - P_{wb})$ (Pruess et al., 2012).

** The productivity index (PI) is calculated as $PI = \frac{2\pi k_h dz}{ln(r_e/r_w) - 3/4}$ (Pruess et al., 2012). The perforation layer thickness, dz, is 20 m, the well radius, r_w, is 0.105 m, and the skin influence is neglected. The effective grid block radius is $r_e = \sqrt{A/\pi}$, where $A = 100$ m^2 is the grid block area.

tween the wellbore and the surrounding rock. Note that the fluid experiences pressure losses due to friction, which are accounted for as described in Adams et al. (2015). The corresponding friction factor is chosen as in Adams et al. (2015). Hence, both specific enthalpy and pressure decrease as the fluid moves up inside the production well. For simplicity, we calculate the enthalpy for only the CO_2 phase, while assuming the liquid phase has negligible influence. This is justifiable when the flow in the wellbore is annular.

The heat flux, q, depends on the formation temperature distribution around the wellbore compared to the fluid temperature. The conductive heat exchange between the wellbore and the surrounding formation is calculated using the method proposed by Zhang et al. (2011). To keep our calculations simple, we make the following assumptions: (i) the thermal resistances between the cased well and the formation is negligible because of the high thermal conductivity of casing metals and (ii) vertical conductive heat flow within the formation is negligible (Zhang et al., 2011). Convective heat transfer for each well element is determined as presented by Randolph et al. (2012), using the assumption that convective heat transfer outside the wellbore is negligible because of the low-permeability, overlying caprocks.

The wellbore model provides the approximate values of the temperature and pressure of the produced fluid (in this case, only the CO_2 phase) as it reaches the wellhead, which also serve as the input values for calculating the enthalpy of the produced CO_2 phase, used for power generation calculations. The wellbore and power plant model parameters used for this study are presented in Table 2.

2.3. CPG power system model

The direct-CO_2 CPG system can be modeled in at least two ways: as a direct-CO_2 thermosiphon-only or as a direct-CO_2 pumped cycle, where the latter may yield somewhat more net power, however, this effect is typically not pronounced (Adams et al., 2014, 2015). Therefore, we model the simpler direct-CO_2 thermosiphon-only CPG system,

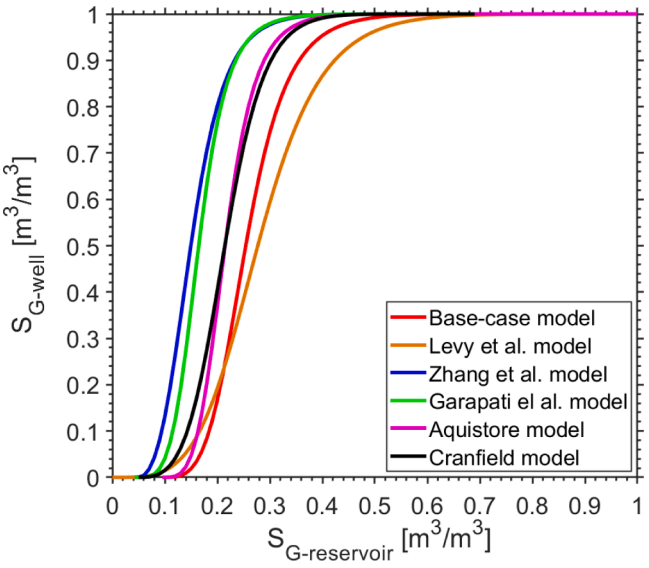

Fig. 8. The calculated CO_2 saturation in the production well, $S_{G\text{-well}}$, for a given CO_2 reservoir saturation in the pore space surrounding the production well inlet, $S_{G\text{-reservoir}}$, for different published reservoir models, i.e. the base-case model (this paper), Levy et al. model (Levy et al., 2018), Zhang et al. model (Zhang et al., 2016), Garapati et al. model (Garapati et al., 2015), Aquistore model (Guyant et al., 2015), and Cranfield model (Delshad et al., 2013).

employing the analysis presented in Adams et al. (2015). As no pump or compressor is used in a thermosiphon-only CPG system, the flow of CO_2 is entirely generated by the CO_2 density difference between the injection and production wells (Adams et al., 2014).

During the CPG stage, once the CO_2 reaches the land surface, via the production well, the supercritical/gaseous CO_2 component of the produced fluid is separated from the liquid water in a water-CO_2 separator. The separated CO_2 is expanded through a two-phase turbine, and power is generated via a generator. The CO_2 that has passed through the turbine is cooled and condensed to the liquid phase, using a cooler/condenser, and it is reinjected into the reservoir.

The electric power output of the turbine, P_t [W_e], for the direct-CO_2 system, is calculated as the product of the CO_2 mass flowrate, $\dot{m}_G$, and the difference between the turbine inlet, h_{in}, and outlet, h_{out}, enthalpies of the fluid (Eq. (9)), where the outlet enthalpy is calculated using an isentropic turbine efficiency of $\eta_{ie} = 78.0\%$ (Ezekiel et al., 2020),

$$P_t = \dot{m}_G \cdot (h_{in} - h_{out}). \quad (9)$$

The net power, P_{net} [W_e], generated by the direct system is then defined by

$$P_{net} = P_t - P_{co} - P_{pump}, \quad (10)$$

where P_{co} and P_{pump} are the parasitic cooling/condensing power and pump power, respectively, required to operate the power plant, where $P_{pump} = 0$ for the thermosiphon-only CPG system considered here. The heat extraction rates of the cooling/condensing towers are equal to the products of the CO_2 mass flowrate and the difference between the fluid enthalpies at the inlet, $h_{in,c}$, and outlet, $h_{out,c}$, of the condenser. Eq. (11) provides the parasitic power requirements of the cooling/condensing towers, where the parasitic load fraction, i.e. the ratio of the parasitic energy load [kW_e] to the heat-rejection energy [kW_{th}], is set to $\lambda_p = 0.03$ (details on the parasitic load fraction can be found in Section 2 of the Supplemental Information in Adams et al., 2015),

$$P_{co} = \dot{m}_G \cdot (h_{in,c} - h_{out,c}) \cdot \lambda_p. \quad (11)$$

As part of the base-case parameters used in this study, the temperature and pressure of the cooled and condensed CO_2 at the CO_2 reinjection

Table 3
Reservoir parameters of selected CO_2-based geothermal and/or CO_2 storage models. Here, S is the water salinity, S_r is residual saturation, m is the van Genuchten parameter, k_r is relative permeability, and n is the Brooks-Corey pore-size-distribution index for the gas (G) and the liquid (L) phases. (Garapati et al., 2015; Guyant et al., 2015; Levy et al., 2018; Zhang et al., 2016; Delshad et al., 2013).

Model	T (°C)	P (MPa)	S (-)	S_{Lr}	S_{Gr}	van-Genuchten	Brooks-Corey			
						m	k_{rG} max	k_{rL} max	n_L	n_G
Garapati et al. (2015)	100	25	0.2000	0.30	0.05	0.46				
Aquistore model (Guyant et al. (2015))	100	35	0.2500	0.40	0.10	0.70				
Levy et al. (2018)	225	22.5	0.0001	0.05	0.01	0.65				
Zhang et al. (2016)	150	35	0.1015	0.30	0.05		1.0	0.35	6.0	2.0
Cranfield model (Delshad et al., 2013)	125	32	0.1500	0.40	0.05		0.8	1.00	4.2	2.6
Base case	100	25	0.1500	0.25	0.10	0.77				

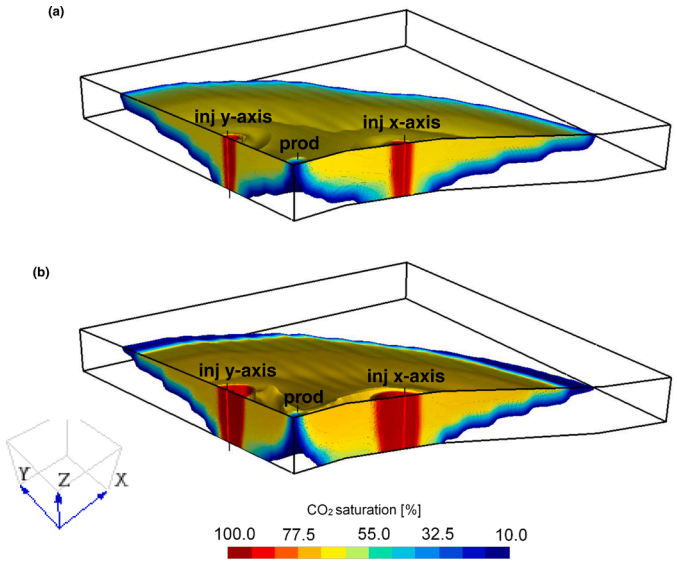

Fig. 9. Quarter model showing the CO_2 saturation in the pore space before (a) and after (b) the CPG stage. Note that the parts of the models with CO_2 saturations less than $S_{G\text{-reservoir}} = 0.1$ have been blanked. The model is exaggerated by a factor of 2.5 along the z-axis.

wellhead is considered to be 15 °C (i.e. an approach temperature of 7 °C + an ambient temperature of 8 °C) and 5.6 MPa, respectively.

3. Results

3.1. Calculating the CO_2 saturation in the production well

Determining the CO_2 saturation (i.e. volume fraction) in the well, $S_{G\text{-well}}$, is important for the characterization of the fluid flow regime existing at the bottom of the production well at any given time. Fig. 8 shows the results of the CO_2 saturation in the well for the base-case model (Table 3) used for this study and five different models of published CO_2-based geothermal energy extraction and/or CO_2 storage studies in deep aquifer systems. Their respective reservoir and fluid parameters are shown in Table 3. The density and dynamic viscosity of the brine solutions are calculated using the Haas (1976) and Phillips et al. (1981) correlations, respectively.

One can see from Fig. 8 that, owing to its low viscosity compared to brine at typical CPG reservoir conditions, the flux of CO_2 into the well is significantly higher than that of water when the CO_2 saturation in the reservoir pore space surrounding the production well inlet is greater than about 0.30 for all cases. For example, for our base case, a CO_2 reservoir pore-space saturation, $S_{G\text{-reservoir}}$, of about 55.0% yields a CO_2 saturation of >98.0% in the production well.

The differences between the various cases shown in Fig. 8 stem primarily from differences in the relative permeability–saturation constitutive relationships used in each case (van Genuchten or Brooks-Corey parameters in Table 3) and the residual water saturation values. Hence, the higher the residual water saturation and the more homogenous the pore-size distribution in the reservoir pore space, the greater the CO_2 volume fraction (and mass fraction) in the well. The effect of temperature, pressure, and salinity also contribute to this effect, but to a lesser degree.

3.2. Base-case simulation results

Using the base-case parameters listed in Table 1, where the injection-to-production well distance in the reservoir is 500 m, the CO_2 plume establishment (PE) stage lasts about four years and requires a total of 15.5 Mtons of CO_2 injected through the four injection wells. Fig. 9a shows the CO_2 gas saturation in the reservoir at the end of the PE stage.

Fig. 10a shows that when the production well is opened (at time = t_0), the CO_2 saturation around the production well decreases from 55.0% to the lowest value of 32.0% because of the water upconing effect. This time of lowest CO_2 saturation in the reservoir's pore space around the inlet of the production wells is referred to in this study as the critical time, t_{crit}. Afterwards, the pore-space CO_2 saturations around the production well inlets begin to increase. After 40 years of fluid production, the CPG stage ends. At this point (t_{end}), the pore-space CO_2 saturations around the production well inlets reach 47.5%. The CO_2 saturation in the reservoir at this point is shown in Fig. 9b. Fig. 10a also shows that the maximum flowrate of 30 kg/s/well is achieved after 5.5 years of CO_2 production. Fig. 10b shows that the mass fraction of CO_2 entering the production well decreases from 0.99 (at t_0) to 0.61 (at t_{crit}). It can be observed (Fig. 10b) that the conditions in the wellbore never reach the slug/churn transition line. Hence, the fluid flows in the desired annular flow regime throughout the simulated 40 years. At the end of the CPG stage, the cool CO_2 front has almost arrived at the location of the production well (Fig. 11).

Fig. 10c shows that the total net power generated for the base case decreases from 0.40 MW_e at the start of fluid production and CO_2 circulation during the CPG stage to about 0.30 MW_e at t_{crit}. The net power then increases to a peak value of 0.80 MW_e after 10 years. At this time, the maximum mass flowrate and a high mass/volume fraction of CO_2 have been achieved. The continuous decline in temperature then leads to a steady power decrease down to about 0.40 MW_e at the end of fluid production (Fig. 10c). For this small-scale example problem, the average net power generated is 0.58 MWe (0.202 GWe-h in 40 years).

3.3. Variation of operational parameters

To optimize the overall performance of the system, by minimizing the amount of water entering the production well and maximizing power output, we investigate how the system responds to changes in three operational parameters that must be chosen by the geothermal power plant operator and compare these results to those of the base case. The three operational parameters are:

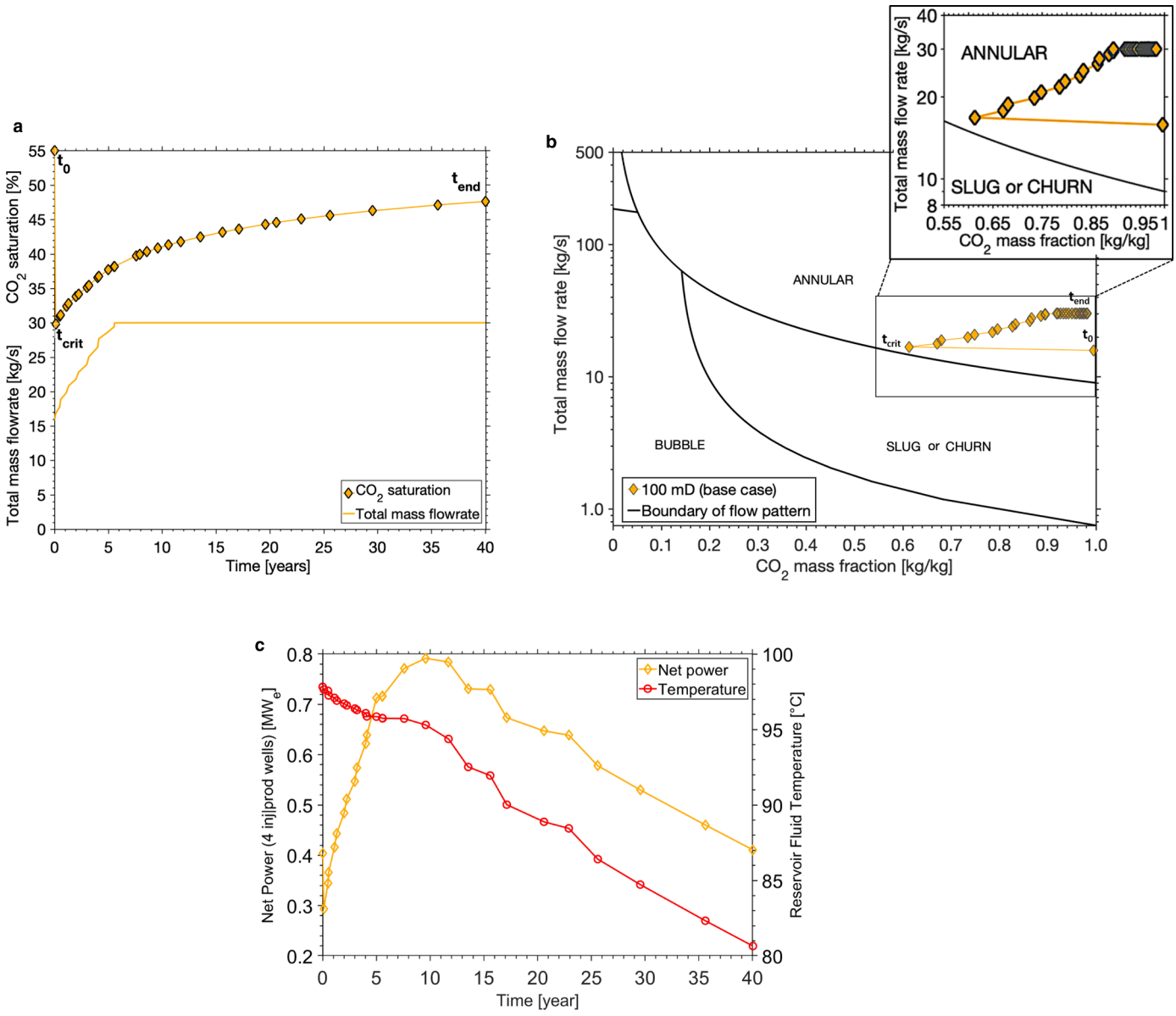

Fig. 10. CPG simulation results for the base case. (a) Time series of the total fluid mass flowrate (per well) and changes in CO_2 saturation in the pore space surrounding the production well inlet, $S_{G\text{-reservoir}}$, (b) Bottom wellbore flow regimes, determined by the total fluid mass flowrate (per well) and CO_2 mass fraction in the production well. The inset figure shows an enlarged region of the plot. (c) Time series of net electric power generation and the reservoir fluid temperature, employing the 4 injection-production well pairs.

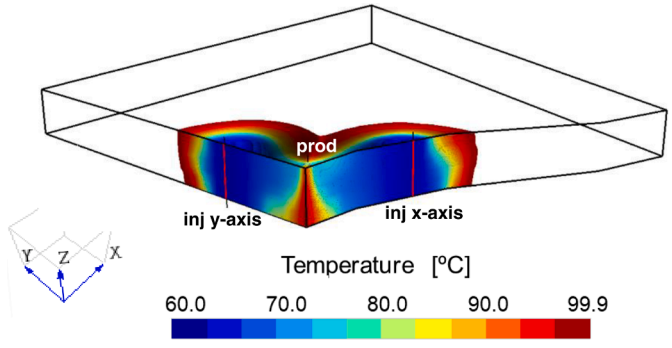

Fig. 11. Quarter (base case) model, showing the temperature distribution in the reservoir at the end of the CPG stage. Note that the part of the model with the temperature equal to the initial temperature of 100 °C has been blanked. The model is exaggerated by a factor of 2.5 along the z-axis.

i Maximum fluid production rate.
ii Admissible reservoir fluid-pressure reduction.
iii Production well pipe diameter.

For all cases, the amount of CO_2 injected, and the duration of the CO_2 plume-establishment (PE) stage are the same as that of the base case.

3.3.1. *Maximum fluid production rate*

For the first permutation of this sensitivity analysis, the maximum circulation flowrate is varied: 20 kg/s/well, 25 kg/s/well, 30 kg/s/well (base case), 35 kg/s/well, and 40 kg/s/well. In all cases, the respective CO_2 injection rate is held identical to the maximum fluid production flowrate considered. Using the simplified power-to-mass-flowrate model (Fig. A1), these maximum circulation flowrates are chosen such that their estimated power outputs lie within 80.0–100.0% of the maximum. The lower two variations are lower than the estimated optimum flowrate, while the higher two flowrates are slightly higher.

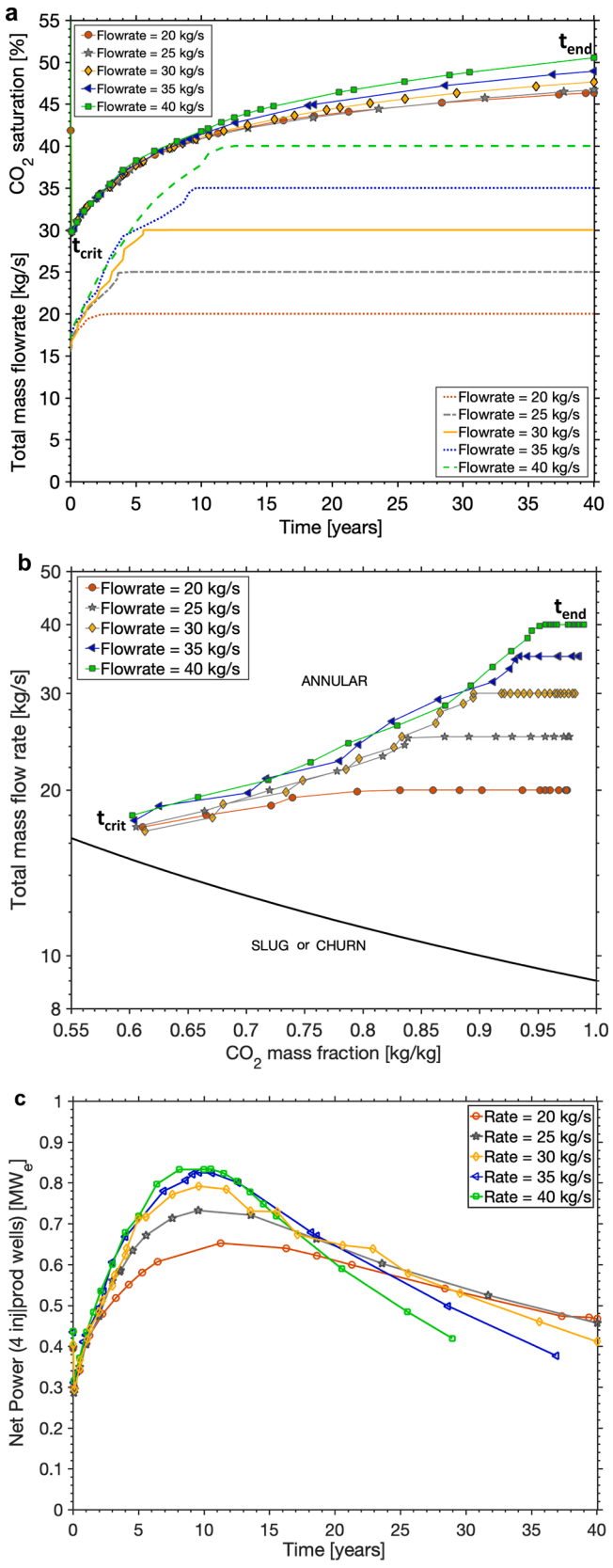

Fig. 12. CPG simulation results for different maximum fluid production rates per well, showing (a) the time series plot of the total fluid mass flowrate and changes in CO_2 saturation in the pore space around the production well inlet, (b) the bottom wellbore flow regime, and (c) the time series of net electric power generation.

Table 4
CPG simulation results for the different operational and reservoir parameters, showing the average net electric power generated (in MW_e), average net electrical energy generated (in GW_e-h), the wellbore simulation end time, t_{end} (in years, where the check symbol, √, means that the simulation completed all 40 years), the CO_2 saturation entering the production well, $S_{G\text{-well}}$, at t_{crit}, when $S_{G\text{-well}}$ is at its lowest value, the CO_2 mass fraction, M_G, at t_{crit}, and the mass flowrate of CO_2, $\dot{m}_G$ (in kg/s/well), at t_{crit}.

	Average net power	Average net energy	End time	$S_{G\text{-well}}$	M_G	$\dot{m}_G$
Flowrate						
20 kg/s	0.500	0.175	√	0.761	0.611	10.002
25 kg/s	0.536	0.188	√	0.757	0.606	10.139
30 kg/s	0.575	0.202	√	0.754	0.604	10.156
35 kg/s	0.595	0.193	37.00	0.755	0.605	10.643
40 kg/s	0.630	0.160	29.00	0.753	0.603	10.758
ΔP						
3 MPa	0.524	0.184	√	0.802	0.680	6.832
5 MPa	0.590	0.207	√	0.771	0.632	8.701
7 MPa	0.575	0.202	√	0.754	0.604	10.156
9 MPa	0.526	0.184	√	0.746	0.585	12.423
Well diameter						
0.11 m	0.235	0.006	3.00	0.760	0.614	9.667
0.21 m	0.575	0.202	√	0.754	0.604	10.156
0.33 m	0.603	0.211	√	0.751	0.597	11.101
0.41 m	0.599	0.210	√	0.750	0.594	11.684
Anisotropy						
kh/kv = 1	0.575	0.202	√	0.754	0.604	10.156
kh/kv = 2	0.554	0.194	√	0.838	0.720	11.577
kh/kv = 4	0.589	0.106	20.60	0.905	0.824	17.127
kh/kv = 8	0.635	0.081	14.50	0.952	0.906	23.293
kh/kv = 10	0.651	0.091	16.00	0.961	0.922	27.664
VG parameter						
VG_p = 0.65	0.490	0.172	√	0.768	0.624	9.571
VG_p = 0.77	0.575	0.202	√	0.754	0.604	10.156
VG_p = 0.97	0.706	0.248	√	0.815	0.728	15.596

Fig. 12a shows that the time required for the system to reach the prescribed maximum fluid production rate increases as the required production flowrate increases. The case with a 20 kg/s/well flowrate takes about 1.27 years, while that with a 40 kg/s/well flowrate takes up to 10.5 years to reach the required flowrate. Also, Fig. 12a shows an equal decrease in the original CO_2 saturation in the pore space surrounding the production well inlet of 55.0% to about 30.0% at the critical time, t_{crit}, for all flowrate cases since they all have the same pressure drawdown at the start of fluid production. Afterwards, the CO_2 saturation increases with time with the highest flowrate (40 kg/s/well) having the highest CO_2 saturation at the production well at the end of the simulation, t_{end}. This is because the CO_2 saturation in the reservoir increases as the CO_2 injection rate increases.

Note that for the sake of clarity, in Fig. 12b, we only show the results starting from the critical time, t_{crit}, to the end time, t_{end}, and do not show the results from t_0, as we did for the base case (Fig. 10b). Fig. 12b shows that, for all flowrates considered, and at the prescribed admissible pressure drawdown (7 MPa), annular flow can be maintained inside the well, i.e. liquid loading should not occur.

The power generated with time is shown in Fig. 12c. We observe that the peak net power generated increases with increasing flowrate. However, after the peak is reached, there is a steeper decline in net power with increasing flowrate. This indicates that the heat depletion rate increases as the flowrate increases. Table 4 shows that, for the

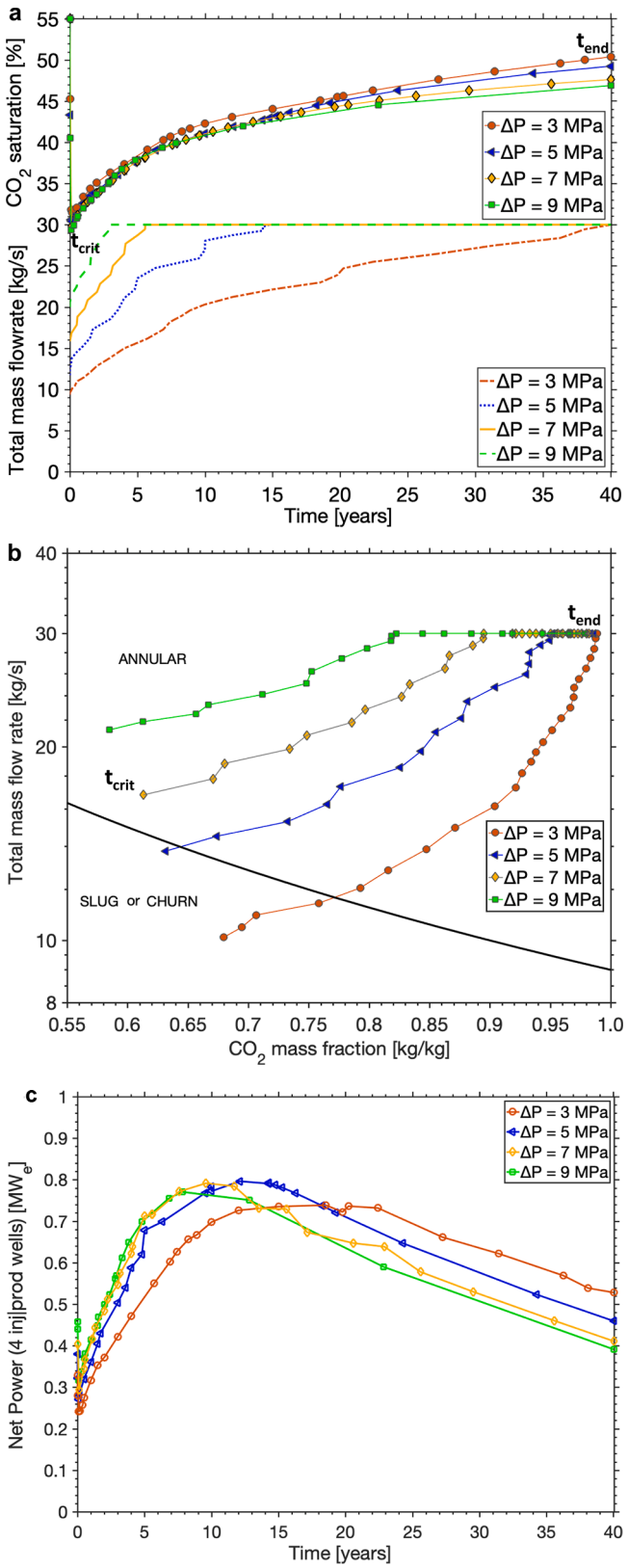

Fig. 13. CPG simulation results for different admissible pressure differences (drawdowns), showing (a) the time series plot of the total fluid mass flowrate (per well) and changes in CO_2 saturation in the pore space around the production well inlet, (b) the bottom wellbore flow regime, and (c) the time series of the net electric power generation.

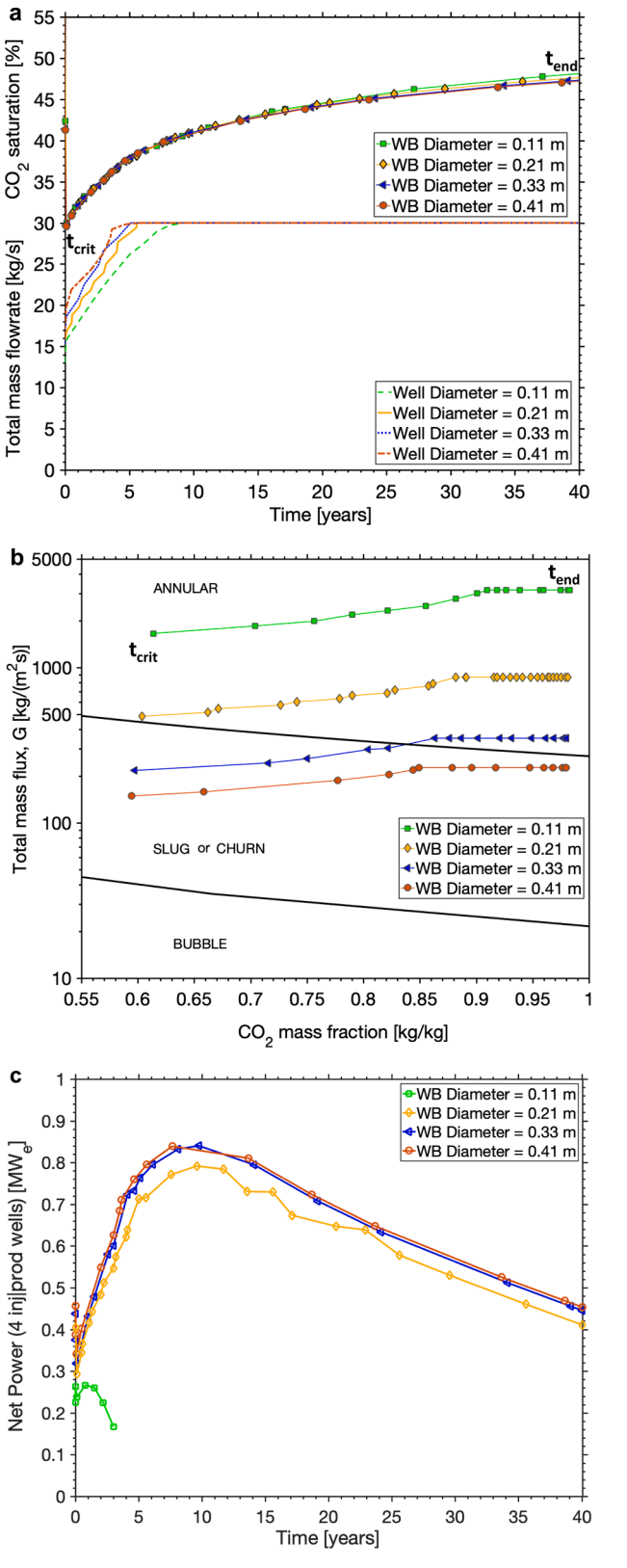

Fig. 14. Simulation results for different production well (WB) pipe diameters, showing (a) the time series plot of the total fluid mass flowrate (per well) and changes in pore-space CO_2 saturation around the production well inlet, (b) the bottom wellbore flow regime, determined by the total mass flux (G) and the CO_2 mass fraction in the production well, (c) the time series of net electric power generation.

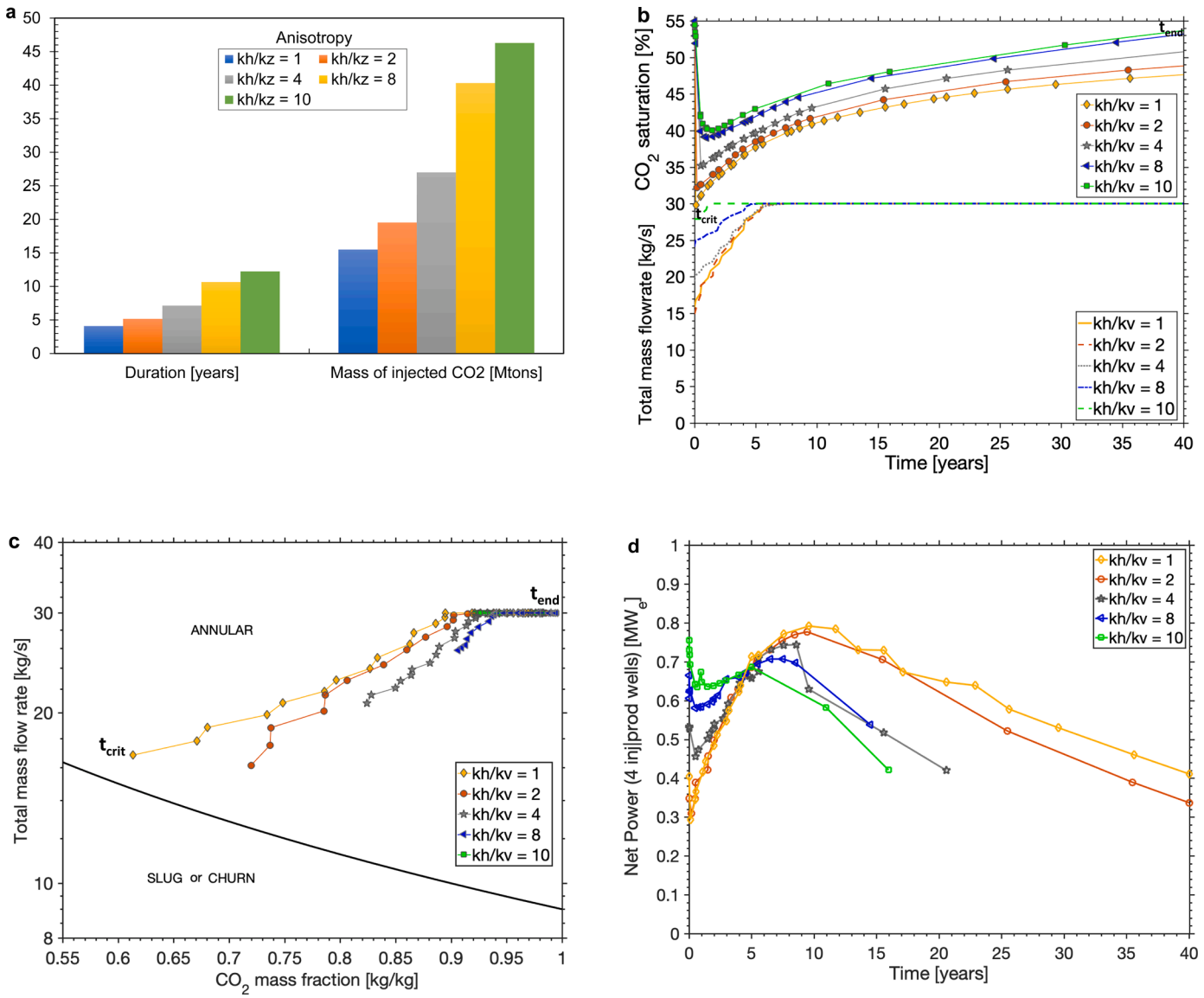

Fig. 15. CPG simulation results for different reservoir anisotropies of horizontal, k_h, to vertical, k_v, permeability, showing (a) the duration and mass of CO_2 injection during the CO_2-plume establishment (PE) stage, (b) time series plot of the total fluid mass flowrate (per well) and changes in CO_2 saturation in the pore space around the production well inlet, (c) the bottom wellbore flow regime, and (d) time series of net electric power generation.

simulation period considered, the average net power generated increases with the flowrate, regardless of the increasing heat depletion rate. However, due to the high pressure (frictional) loss associated with high flowrates in the well pipes, there is a large pressure and temperature drop of the produced CO_2 in the wellbore. At some point in time, the saturation vapor pressure of CO_2 is reached (which the wellbore model cannot handle), causing the wellbore simulation to stop. At this point, we assume that CO_2 can no longer be favorably produced. This is observed for the higher flowrates of 35 and 40 kg/s/well as the simulation did not reach the desired 40 years end time (Table 4). Hence, even though these two flowrates generated higher average net power than the base case, the average net energy generated is less. This indicates that there is an upper bound to the maximum flowrate when the reservoir is depleted too rapidly.

3.3.2. *Admissible reservoir fluid-pressure reduction*

The admissible reduction in reservoir fluid pressure is varied as: 3, 5, 7 (base case), and 9 MPa pressure difference, ΔP, between the lowest pressure in the reservoir and the initial pressure. In a real-field application, this value will have to be chosen so as not to damage the caprock. Acceptable values depend on the structural setting and the caprock type. Fig. 13a shows that the total fluid (CO_2 and water) mass flowrate increases faster as the pressure difference increases. The case of 9 MPa pressure difference achieves the maximum flowrate of 30 kg/s/well in 2.8 years, compared to the base case pressure difference (7 MPa) example, which takes 5.5 years. For a pressure difference of 3 MPa, the total fluid mass flowrate of 30 kg/s/well is not reached in 40 years. This implies that CO_2 additions are required during CO_2 injection throughout the 40-year CPG operation in this case. The CO_2 saturation in the pore space around the production well inlet decreases more strongly with increasing fluid-pressure difference (Fig. 13a).

There are two opposing effects here: lower admissible reservoir pressure reductions lead to less water production but also lead to low initial flowrates in the production well (decreasing the likelihood for annular flow to occur). The flowrates achieved in the well at early times for both the 3 MPa and 5 MPa cases are lower than the critical flowrate needed to maintain annular flow (Fig. 13b). Greater admissible reservoir pressure reductions tend to draw in more water into the production well, but also result in high flowrates in the production well, necessary to transport the water droplets up and out of the well (Fig. 13b).

The power generation results in Fig. 13c show that the heat depletion rate increases with ΔP. For the two cases that achieved annular flow all through the 40-year simulations, Table 4 shows that the average net power output and energy generated for the base case ΔP = 7 MPa are higher than that of ΔP = 9 MPa. Furthermore, an upper limit of the admissible reservoir pressure reduction typically exists, which results from considerations concerning caprock integrity (Vialle et al., 2019).

3.3.3. Production well pipe diameter

Large production well pipe diameters promote high fluid flowrates and low heat losses to the surrounding rock formation during fluid ascent. However, small pipe diameters result in higher CO_2 superficial velocities for a given flowrate, necessary to avoid the slug/churn flow regime in the production well. The production well pipe diameter is therefore an important optimization parameter for CPG systems. Hence, we vary the production well pipe diameter, taking on the values of 0.11 m, 0.21 m (base case), 0.33 m, and 0.41 m, which closely match the well pipe diameter values used in Adams et al., 2015.

The achieved wellbore flowrate slightly increases with increasing well pipe diameter (Fig. 14a). The well diameter of 0.11 m takes about an additional 3.5 years to reach the 30 kg/s/well flowrate, compared to the well diameter of 0.41 m. The CO_2 saturation profile over time is almost the same for all cases considered. The larger well pipe diameters (0.33 m and 0.41 m) cause flow that is partially or fully in the slug/churn flow regime (Fig. 14b). Note that in Fig. 14b, as opposed to the previous cases, the total mass flux, G (i.e. the total mass flowrate divided by the wellbore cross-sectional area), is plotted as a function of CO_2 mass fraction. The flow pattern transition lines change with varying well diameter, and to maintain a unique boundary transition line, the total mass flux is used here. Fig. 14b shows that G needs to be above about 500 kg/s/m^2 to start and stay in the annular flow regime. Fig. 14b also shows that, as the total mass flowrate increases, the plot for the well pipe diameter of 0.33 m moves from the slug/churn flow regime into the annular flow regime. However, throughout the 40 years of CPG simulation time, the largest well pipe diameter case does not reach the critical flowrate needed to achieve annular flow even at the maximum total mass flowrate.

Fig. 14c shows that the power generated by the smallest well pipe diameter of 0.11 m decreases drastically from 0.26 MW_e until the simulation terminates at 0.17 MW_e after only 3 years. This is because of the high pressure and heat losses encountered in the small-diameter production well, with relatively high flowrates. Due to this large pressure and temperature drop of the produced CO_2, the saturation vapor pressure of CO_2 is reached (and out of range for the wellbore model thermophysical properties). The other three well pipe diameters result in very similar power output curves.

3.4. Variation of reservoir parameters

In this section, we carry out numerical simulations to investigate the influence of two key reservoir parameters (permeability anisotropy and relative permeability) on the flow regime in the production well and on electric power generation. For all simulations, except for the respective parameters considered, the reservoir and fluid parameters are the same as in the base case (Table 1).

Varying these reservoir characteristics changes the amount of time needed to complete the CO_2 plume establishment stage. Hence, for the PE stage, we present the various simulation results in terms of the duration of the PE stage and the mass of CO_2 injected. The results serve as the initial conditions for the simulation of the CPG stage for the different cases described in this paper.

3.4.1. Reservoir-permeability anisotropy

Permeability anisotropy is implemented here by reducing the value of the vertical permeability, k_v, while keeping the horizontal permeability, k_h, constant at 100 mD. This way, we stay as close as possible to the base case, and the variations here focus on the importance of vertical flow.

As shown in Fig. 15a, the duration of the PE stage and the mass of injected CO_2 required to reach a CO_2 saturation of 55.0% in the pore space around the production well inlet increase as the anisotropy of the reservoir permeability increases. Fig. 15b shows that the drop in the CO_2 saturation around the production well (due to fluid-pressure drawdown) decreases with increasing permeability anisotropy (for $k_v < k_h$). This is mainly because, due to the lower vertical permeability, water upconing to the well perforation (at the top of the reservoir) is reduced. Accordingly, the maximum flowrate is more readily achieved at higher CO_2 saturations. These factors favor an annular flow regime (Fig. 15c). However, from a power-generation perspective, higher permeability anisotropies lead to higher heat depletion rates, lower peaks in power generation, and a sharp decrease in power generation with time (Fig. 15d), requiring re-optimizing the flowrate.

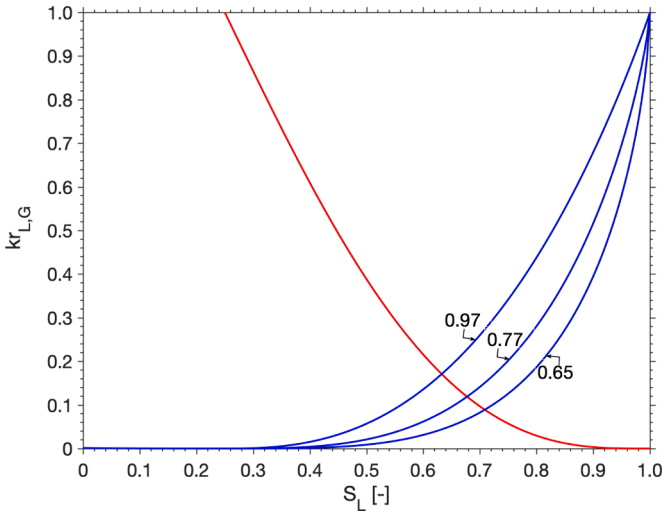

Fig. 16. Relative permeability-liquid saturation curves for different van Genuchten (VG) parameters. The supercritical/gaseous CO_2 relative permeability curve (red line) is the same for all VG parameters.

3.4.2. Relative permeability

Here, we vary the van Genuchten (VG) parameter, m, between 0.65 and 0.97. This corresponds to mildly heterogeneous (0.65) to highly homogeneous (0.97) pore-size distributions (compare with values in Ghezzehei et al., 2007). For comparison, Barea sandstone, which is considered a very homogeneous rock, has a van Genuchten parameter of 0.89, as reported in Ghezzehei et al., 2007. Fig. 16 shows relative permeability versus water saturation curves for the different VG parameters considered in this study. The CO_2 relative permeability remains the same for all values of m.

Fig. 17a shows that it takes longer, and that a larger mass of injected CO_2 is required, for low values of the VG parameter (0.65) to reach a CO_2 saturation of 55.0% in the pore space around the production well inlet. Fig. 17b shows that the decrease in CO_2 saturation is similar for all cases. At lower m, the water relative permeability is very low (for a CO_2 saturation of 55.0%), as shown in Fig. 16, and the water phase is almost immobile, which means that the water hardly flows into production well. Fig. 17c shows that all cases achieved annular flow conditions in the production well, with the case of $m = 0.97$ having the highest CO_2 mass fraction and flowrate at t_{crit}.

The net power generation results presented in Fig. 17d show that the net power peaks at an earlier time and the average net power output (Table 4) increases as the value of the VG parameter increases.

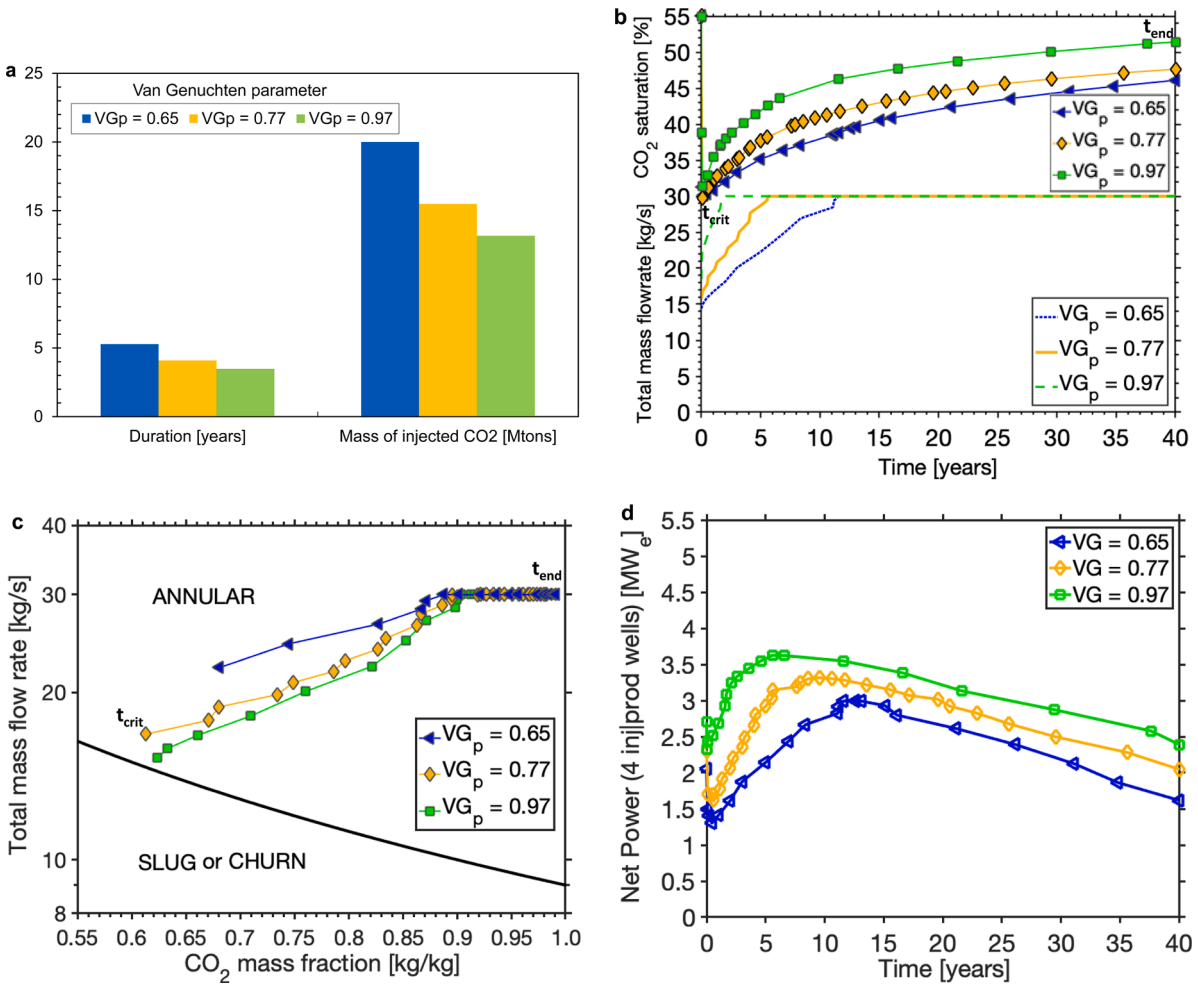

Fig. 17. CPG simulation results for different van Genuchten relative permeability parameters, showing (a) the duration and mass of CO_2 injected during the CO_2-plume establishment (PE) stage, (b) time series plot of the total mass flowrate (per well) and changes in CO_2 saturation in the pore space around the production well inlet, (c) bottom wellbore flow regime, and (d) time series of net electric power generation.

3.5. Minimum superficial CO_2 velocity as a design parameter

To design a CPG system that avoids water accumulation, and thus maintains annular flow, in the production well, the velocity of CO_2 in the production well must be higher than the minimum superficial CO_2 velocity, calculated with Turner's model (Turner et al., 1969). This is incorporated in the flow-regime equations of Taitel et al. (1980) and indicated as Line C in Fig. 4. To determine how this minimum value changes with reservoir depth, for a CPG system, we plot the minimum superficial CO_2 velocity with depth (800–3400 m) in Fig. 18a. We apply an approximately standard continental-crust geothermal temperature gradient of 37 °C/km and assume a constant salt mass fraction of 0.15 in the water at all depths, which can be used to calculate the density of brine (Haas, 1976) and the fluid pressure gradient at the various depths considered. For the range of pressures and temperatures considered at these depths, the interfacial tension of the CO_2-water system is determined using the empirical exponential equation described by Bachu and Bennion (2009). Fig. 18a shows that the minimum superficial CO_2 velocity, for the described CPG system, is around 0.44 – 0.46 m/s if the depth is greater than 1500 m and between 0.46 and 0.70 m/s for depths between 1500 m and 800 m.

A more practical design parameter than the superficial CO_2 velocity is the bulk velocity of the fluids in the well, i.e. the sum of the superficial velocities of water and CO_2. The minimum bulk velocity necessary to maintain annular CO_2 flow in the borehole depends on the composition of the fluids in the borehole. For a given volume fraction (saturation) of CO_2 in the production well, the minimum bulk velocity, U_{total}, can be calculated from the minimum CO_2 superficial velocity by

$$U_{total} = U_{S,G}/S_{G-well}. \quad (12)$$

Fig. 18b shows the ratio of bulk velocity, U_{total}, to the superficial CO_2 velocity, $U_{S,G}$, for CO_2 saturations in the production well, $S_{G\text{-well}}$, ranging from 0.5 to 1. For example, when $S_{G\text{-well}} = 0.5$, the figure indicates that the minimum bulk velocity required in the borehole to maintain annular fluid flow is 0.9 m/s for depths greater than 1500 m and between 0.9 m/s and 1.4 m/s for shallower depths, ranging from 1500 m to 800 m. Irrespective of the value of $S_{G\text{-well}}$, the minimum CO_2 superficial velocity as shown in Fig. 18a should be achieved in order to ensure annular flow.

3.6. Application to the Cranfield CO_2-based geothermal field experiment

We can apply the findings of this study to gain insights into the problems with liquid water in the production well, postulated as one of the factors that led to the failure of the Cranfield (Mississippi, USA) CO_2 thermosiphon-alone circulation field test (Adams et al., 2021a). However, as in the Introduction section, we emphasize that a thermosiphon is not necessary for successful CPG operations, as also stated by Adams et al. (2021a) in the conclusions: "A self-sustaining thermosiphon is not necessary for the successful operation of a CO_2-based geothermal system. In the event of water accumulation in the production well, the system may be pumped to circulate the hot geologic fluid to the surface,

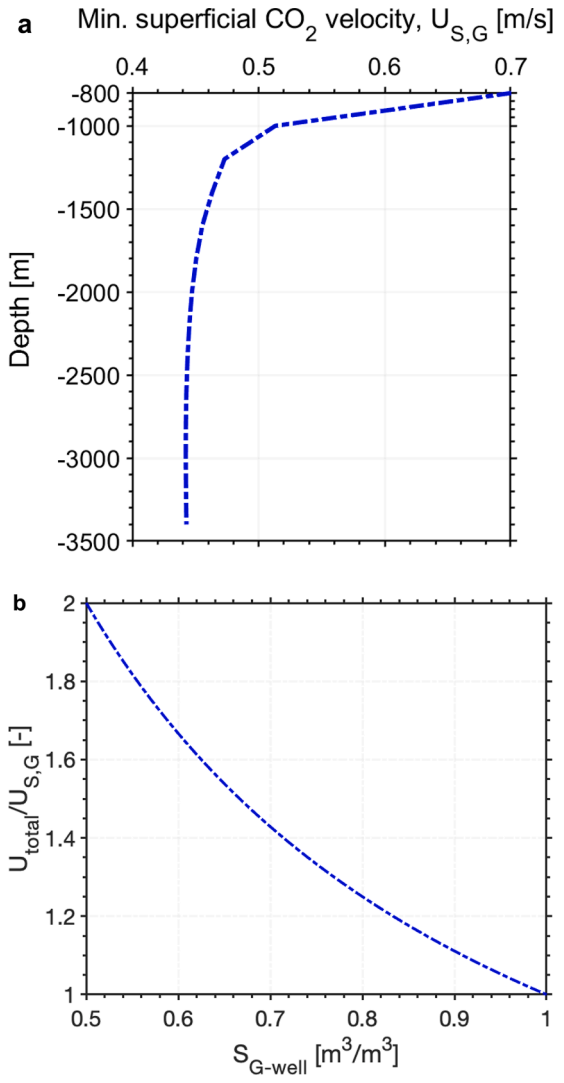

Fig. 18. (a) Variation of the minimum superficial CO_2 velocity with depth for a CPG system with a geothermal temperature gradient of 37 °C/km and a dissolved salt mass fraction in the water phase of 0.15. (b) Variation of the ratio of bulk velocity, U_{total}, to the superficial CO_2 velocity, $U_{S,G}$, as a function of the CO_2 saturation in the production well, $S_{G\text{-well}}$.

just like a water-based geothermal system." Apart from the factors (i.e. homogeneous reservoir with no clay lens, relatively high reservoir temperature, well-tubing insulation, smooth pipe with low flow resistance) discussed by Pan et al. (2018) necessary to sustain the thermosiphon at the Cranfield field test, it is also important to optimize the production fluid flowrate. During the field test, the maximum flowrate achieved by venting the production well was 2.1 kg/s during Venting #3 (Freifeld et al., 2016). However, using Cranfield's reservoir and fluid properties (presented in Table 3) and the production wellbore diameter of 0.14 m used at the Cranfield site (see Freifeld et al., 2016 and Pan et al., 2018 for more details), we calculate that a minimum mass flowrate of 3.95 kg/s (i.e. with a minimum superficial CO_2 velocity of 0.43 m/s) is required to achieve annular flow in the wellbore that would sustain a thermosiphon (Fig. 19).

The minimum mass flow rate required to achieve annular flow increases as the mass fraction of water in the well increases (Fig. 19). From this point of view, the low mass flowrate achieved (i.e. a maximum of

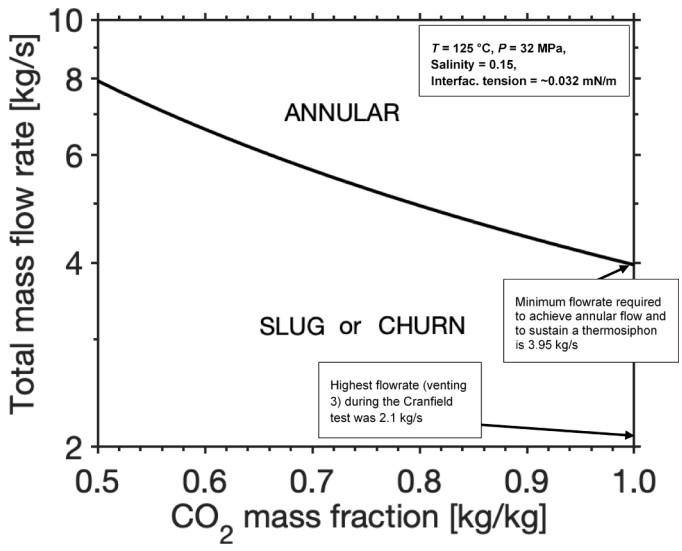

Fig. 19. The production well flow regime for the Cranfield CO_2 circulation test in the USA, as a function of total fluid mass flowrate and CO_2 mass fraction. The minimum flowrate required to achieve annular flow in the wellbore that would sustain a thermosiphon is 3.95 kg/s. The highest total mass flowrate actually achieved during the Cranfield CO_2 circulation test was only 2.1 kg/s (Freifeld et al., 2016).

2.1 kg/s) during the Cranfield test is not enough to prevent water accumulation in the production well over time (liquid loading). Almost twice that maximum flowrate of 2.1 kg/s would have been necessary to ensure any entrained water is lifted out of the production well, achieving annular flow and supporting the CO_2 thermosiphon that was being tested at the Cranfield site.

4. Discussion

The coupling of the reservoir, production wellbore, and power systems makes it possible to optimize the production flowrate in such a way as to ensure annular flow in the production well without unduly compromising CPG power output. The base-case results show that the largest water production occurs at the start of the CPG stage and may lead to slug/churn flow at this early time. Slug/churn flow in the production well causes pressure fluctuations, undermines CO_2 circulation and the thermosiphon, and leads to a higher fluid density in the production well. Thus, a CO_2 pump or compressor at the CO_2 injection wellhead may be necessary to maintain the required production well fluid flowrate at the beginning of CPG operations. The operational parameters should be optimized for the given reservoir characteristics to achieve an annular-regime flowrate and maximize a combination of power output and lifetime of the geothermal system. From the cases studied here, the following inferences can be drawn:

- For a fixed fluid mass flowrate or downhole pressure difference, CO_2 velocities decrease with increasing well pipe diameter. This can lead to slug/churn flow in the production well. However, small well pipe diameters yield high fluid pressure and heat losses, which results in lower power generation. Hence, to optimize the system, a production well pipe diameter that can achieve annular flow, while minimizing pressure and heat losses in the production well, is sought. In our study, a production well pipe diameter of 0.21 m results in an optimal fluid flowrate, compared to pipe diameters of 0.11 m, 0.33

m, and 0.41 m. This highlights that the optimization of well pipe diameters should be considered when designing CPG systems.

- When varying admissible reservoir fluid-pressure reductions, our results show that there is a tradeoff between high fluid flowrates and water entering the production well. This tradeoff should be accounted for when determining the optimal flowrate for a CPG system. Relatively high reservoir fluid-pressure reductions lead to high flowrates and hence higher amounts of water entering the production well. However, high total fluid flowrates could be high enough to carry the water out of the well. In addition, higher flowrates lead to faster rates of heat depletion of the reservoir. Finally, the reservoir can only support flowrates that do not cause reservoir pressure drawdowns that could compromise the structural integrity of the caprock.
- Our reservoir parameter sensitivity analysis shows that lower vertical permeabilities (i.e. higher permeability anisotropies) lead to a reduced water upconing effect, meaning that less water is drawn into the production well through its screen. Higher permeability anisotropies also reduce the heat sweep of the plume, decreasing the CPG power plant lifetime. The reservoir-parameter sensitivity analysis also shows that the shapes of the relative permeability curves considerably affect the relative amounts of CO_2 and water entering the production well. Therefore, precise measurements of relative permeability curves for the specific reservoir formation in question are important to improve predictions of CPG performance, particularly at the beginning of the operation (fluid production), when the system is most prone to water entering the production well.

Any produced water needs to be removed from the produced CO_2 stream before CO_2 reinjection into the CPG reservoir, as otherwise the CO_2 injectivity into the geologic reservoir is likely significantly compromised (Garapati et al., 2015).

5. Conclusions

This study highlights the importance of properly designing CO_2-Plume Geothermal (CPG) systems by optimizing the fluid production flowrate to minimize the amount of water entering the production well and maintain annular flow in the production well, while maximizing power generation. We employ a numerical modeling approach that couples the reservoir processes with the well and power plant systems. Using this model, we conduct a flow pattern transition study to determine the flow regime in the CPG production well for a CO_2-brine system for different total fluid mass flowrates and corresponding CO_2 mass fractions. Our findings are as follows:

1) To achieve annular flow in the production well, the required minimum superficial CO_2 velocity is approximately 0.44 – 0.46 m/s if the reservoir depth is greater than 1500 m and between 0.46 and 0.70 m/s for shallower reservoir depths between 1500 m and 800 m. Hence, using these values for a given reservoir depth, the minimum flowrate necessary to achieve annular flow in the production well can generally be estimated.
2) We provide insights into one of the reasons why the CO_2 thermosiphon test at the Cranfield site (USA) was unsuccessful. Using the reservoir properties and well pipe diameter at the Cranfield site, our results show that the minimum CO_2 flowrate, required to achieve annular flow in the production well, is about twice as high as the actual maximum flowrate achieved during the venting stages of the Cranfield test.
3) The results of the operational parameter sensitivity study show that the admissible reservoir fluid pressure drawdown is an important limiting factor for achieving the fluid flowrate in the CPG production well necessary to avoid water accumulation. In addition, the well diameter can be optimized so as to obtain a high CO_2 velocity but low heat and pressure losses in the well.
4) The results of the reservoir parameter sensitivity study show that higher permeability anisotropies tend to reduce the upconing of water to the production well. In addition, relative permeability curves strongly influence the water influx into the production well and the power generation.

CRediT authorship contribution statement

Justin Ezekiel: Methodology, Software, Formal analysis, Investigation, Writing – original draft, Writing – review & editing. **Benjamin M. Adams:** Methodology, Software, Validation, Writing – review & editing. **Martin O. Saar:** Resources, Validation, Writing – review & editing, Supervision. **Anozie Ebigbo:** Conceptualization, Methodology, Software, Formal analysis, Validation, Investigation, Writing – review & editing, Supervision.

Declaration of Competing Interest

The authors declare no conflict of interest.

Acknowledgments

The authors would like to thank the State Secretariat for Education, Research and Innovation (SERI) for a Swiss Government Excellence Scholarships for Foreign Scholars and Artists that supported this study. The Werner Siemens Foundation (Werner Siemens-Stiftung) is also thanked by Martin O. Saar for its support of the Geothermal Energy and Geofluids (GEG.ethz.ch) Group at ETH Zurich, Switzerland. We thank the editors for their excellent support, and we also thank the 4 anonymous reviewers for their excellent feedback on an earlier version of the manuscript, which improved this paper. Any opinions, findings, conclusions, and/or recommendations expressed in this material are those of the authors and do not necessarily reflect the views of the SERI, the Werner Siemens-Stiftung, or ETH Zurich.

Appendix

Power-to-mass-flowrate model

Depending on the mass flowrate, the power generated by a CPG system varies significantly (Adams et al., 2015). It can reduce from the optimum or even become negative. Fig. A1 shows the power generated, using well diameters of 0.11 m, 0.21 m (base case), and 0.33 m, as total CO_2 circulating mass flowrate increases. The CPG power generation

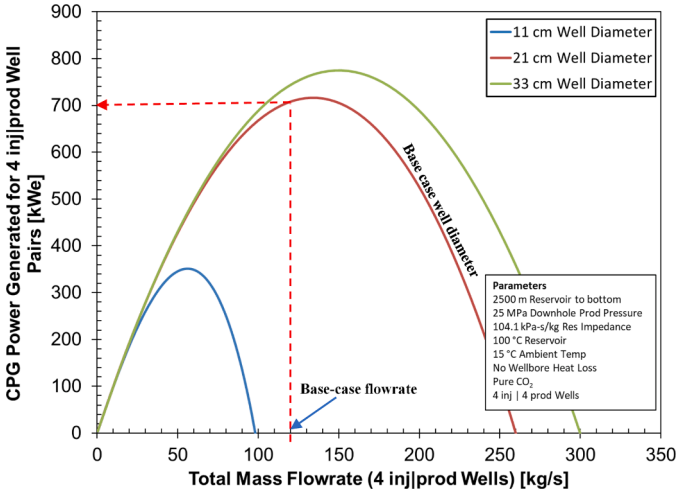

Fig. A1. An example illustrating the CPG power generated by 4 injection-production well pairs at varying total mass flowrates for 3 different wellbore diameters. Heat loss in the wellbore is not considered in this calculation.

calculation was carried out identically to Adams et al. (2015) for a 2.5 km deep reservoir, with the exception of the reservoir impedance, which is 104.2 kPa-s/kg here, and 8 wells were considered instead of the 5 wells in a 5-spot well model. Wellbore heat transfer is not considered in this semi-analytic CPG power generation calculation. This figure is used to choose the base-case total mass flowrate of 120 kg/s for the four injection and production well pairs.

References

Adams, B.M., Fleming, M.R., Bielicki, J.M., Garapati, N., Saar, M.O., 2021a. An analysis of the demonstration of a CO_2-based thermosiphon at the SECARB Cranfield site. In: Proceedings, 46th Workshop on Geothermal Reservoir Engineering. Stanford, California, USA. Stanford University. https://doi.org/10.3929/ethz-b-000467171.

Adams, B.M., Kuehn, T.H., Bielicki, J.M., Randolph, J.B., Saar, M.O., 2015. A comparison of electric power output of CO_2 Plume Geothermal (CPG) and brine geothermal systems for varying reservoir conditions. Appl. Energy 140, 365–377. https://doi.org/10.1016/J.APENERGY.2014.11.043.

Adams, B.M., Kuehn, T.H., Bielicki, J.M., Randolph, J.B., Saar, M.O., 2014. On the importance of the thermosiphon effect in CPG (CO_2 plume geothermal) power systems. Energy 69, 409–418. https://doi.org/10.1016/j.energy.2014.03.032.

Adams, B.M., Vogler, D., Kuehn, T.H., Bielicki, J.M., Garapati, N., Saar, M.O., 2021b. Heat depletion in sedimentary basins and its effect on the design and electric power output of CO_2 Plume Geothermal (CPG) systems. Renew. Energy 172, 1393–1403. https://doi.org/10.1016/j.renene.2020.11.145.

Atrens, A., Gurgenci, H., Rudolph, V., 2009. Exergy analysis of a CO_2 thermosiphon. In: Proceedings of the Thirty-Fourth Workshop on Geothermal Reservoir Engineering. Stanford, California, pp. 1–6.

Bachu, S., Brant Bennion, D., 2009. Interfacial tension between CO_2, freshwater, and brine in the range of pressure from (2 to 27) MPa, temperature from (20 to 125) °C, and water salinity from (0 to 334 000) mg•L−1. J. Chem. Eng. Data 54, 765–775. https://doi.org/10.1021/je800529x.

Bell, I.H., Jäger, A., 2016. Helmholtz energy transformations of common cubic equations of state for use with pure fluids and mixtures. J. Res. Natl. Inst. Stand. Technol. 121, 26. https://doi.org/10.6028/jres.121.011.

Bell, I.H., Wronski, J., Quoilin, S., Lemort, V., 2014. Pure and pseudo-pure fluid thermophysical property evaluation and the open-source thermophysical property library CoolProp. Ind. Eng. Chem. Res. 53, 2498–2508. https://doi.org/10.1021/ie4033999.

Brown, D.W., 2000. A hot dry rock geothermal energy concept utilizing supercritical CO_2 instead of water. In: Proceedings of the Twenty-Fifth Workshop on Geothermal Reservoir Engineering. Stanford, California, pp. 1–6.

Coats, K.H., 1977. Geothermal reservoir modelling. In: SPE Annual Fall Technical Conference and Exhibition. Society of Petroleum Engineers, Denver, Colorado, p. 33. https://doi.org/10.2118/6892-MS.

Coleman, J.L., Cahan, S.M., 2012. Preliminary Catalog of the Sedimentary Basins of the United States: U.S. geological survey open-file report.

Delshad, M., Kong, X., Tavakoli, R., Hosseini, S.A., Wheeler, M.F., 2013. Modeling and simulation of carbon sequestration at Cranfield incorporating new physical models. Int. J. Greenh. Gas Control 18, 463–473. https://doi.org/10.1016/j.ijggc.2013.03.019.

Eccles, J.K., Pratson, L., 2014. A "carbonshed" assessment of small- vs. large-scale CCS deployment in the continental US. Appl. Energy 113, 352–361. https://doi.org/10.1016/j.apenergy.2013.07.002.

Ezekiel, J., Ebigbo, A., Adams, B.M., Saar, M.O., 2020. Combining natural gas recovery and CO_2-based geothermal energy extraction for electric power generation. Appl. Energy 269, 1–21. https://doi.org/10.1016/j.apenergy.2020.115012.

Ezekiel, J., Kumbhat, D., Ebigbo, A., Adams, B.M., Saar, M.O., 2021. Sensitivity of reservoir and operational parameters on the energy extraction performance of combined CO_2-EGR–CPG systems. Energies. https://doi.org/10.3390/en14196122.

Farshad, F.F., Rieke, H.H., 2006. Surface roughness design values for modern pipes. SPE Drill. Complet. 21, 212–215. https://doi.org/10.2118/89040-PA.

Fleming, M.R., Adams, B.M., Kuehn, T.H., Bielicki, J.M., Saar, M.O., 2020. Increased power generation due to exothermic water exsolution in CO2 Plume geothermal (CPG) power plants. Geothermics 88. https://doi.org/10.1016/j.geothermics.2020.101865.

Freifeld, B.M., Pan, L., Doughty, C., Zakem, S., Hart, K., Hostler, S., 2016. Demonstration of geothermal energy production using carbon dioxide as a working fluid at the SECARB Cranfield Site, Cranfield, Mississippi. In: Proceedings, 41st Workshop on Geothermal Reservoir Engineering, pp. 1–14.

Garapati, N., Adams, B.M., Fleming, M.R., Kuehn, T.H., Saar, M.O., 2020. Combining brine or CO2 geothermal preheating with low-temperature waste heat: a higher-efficiency hybrid geothermal power system. J. CO_2 Util. 42, 101323 https://doi.org/10.1016/j.jcou.2020.101323.

Garapati, N., Randolph, J.B., Saar, M.O., 2015. Brine displacement by CO_2, energy extraction rates, and lifespan of a CO_2-limited CO_2-Plume Geothermal (CPG) system with a horizontal production well. Geothermics 55, 182–194. https://doi.org/10.1016/j.geothermics.2015.02.005.

Ghezzehei, T.A., Kneafsey, T.J., Su, G.W., 2007. Correspondence of the Gardner and van Genuchten–Mualem relative permeability function parameters. Water Resour. Res. 43 https://doi.org/10.1029/2006WR005339.

Guyant, E., Han, W.S., Kim, K.Y., Park, M.H., Kim, B.Y., 2015. Salt precipitation and CO_2/brine flow distribution under different injection well completions. Int. J. Greenh. Gas Control 37, 299–310. https://doi.org/10.1016/j.ijggc.2015.03.020.

Haas, J.L., 1976. Thermodynamic properties of the coexisting phases and the thermochemical properties of the NaCl component in boiling NaCl solutions. Geol. Surv. Bull. 1421-B, B1–B70.

He, D., Bai, B., 2014. A new correlation for wet gas flow rate measurement with Venturi meter based on two-phase mass flow coefficient. Meas. J. Int. Meas. Confed. https://doi.org/10.1016/j.measurement.2014.08.014.

IPCC, 2014. Climate change 2014: mitigation of climate change. Contribution of Working Group III to the Fifth Assessment Report of the Intergovernmental Panel on Climate Change Edenhofer, O., R. Pichs-Madruga, Y. Sokona, E. Farahani, S. Kadner, K. Seyboth et al.

IPCC, 2005. IPCC special report on carbon dioxide capture and storage. Prepared by Working Group III of the Intergovernmental Panel on Climate Change M. Bert, O. Davidson, H.C. de Coninck, M. Loos, and L.A. Meyer (eds.). Cambridge University Press, Cambridge.

Lea, J.F., Nickens, H.V., Wells, M.R., 2008. Chapter 1 - introduction. In: Lea, J.F., Nickens, H.V, Wells, M.R.B.T.-G.W.D (Eds.), Gas Well Deliquification, 2nd E. (Eds. Gulf Professional Publishing, Burlington, pp. 1–11. https://doi.org/10.1016/B978-075068280-0.50002-0.

Levy, E.K., Wang, X., Pan, C., Romero, C.E., Maya, C.R., 2018. Use of hot supercritical CO_2 produced from a geothermal reservoir to generate electric power in a gas turbine power generation system. J. CO_2 Util. 23, 20–28. https://doi.org/10.1016/J.JCOU.2017.11.001.

Pan, L., Doughty, C., Freifeld, B., 2018. How to sustain a CO_2-thermosiphon in a partially saturated geothermal reservoir: lessons learned from field experiment and numerical modeling. Geothermics 71, 274–293. https://doi.org/10.1016/j.geothermics.2017.10.004.

Pan, L., Doughty, C., Freifeld, B., Oldenburg, C., 2015. Modeling a CO_2 thermosiphon in a partially saturated reservoir using EOS7CMA. In: Proceedings, TOUGH Symposium 2015. Berkeley, CA. Lawrence Berkeley National Laboratory, pp. 28–30. September.

Phillips, S., Igbene, A., Fair, J., Ozbek, H., Tarvana, M., 1981. A Technical Databook for Geothermal Energy Utilization. Lawrence Berkeley Laboratory Report, p. 12810.

Procesi, M., Cantucci, B., Buttinelli, M., Armezzani, G., Quattrocchi, F., Boschi, E., 2013. Strategic use of the underground in an energy mix plan: synergies among CO_2, methane geological storage and geothermal energy. Latium Region case study (Central Italy). Appl. Energy 110, 104–131. https://doi.org/10.1016/J.APENERGY.2013.03.071.

Pruess, K., 2008. On production behavior of enhanced geothermal systems with CO_2 as working fluid. Energy Convers. Manag. 49, 1446–1454. https://doi.org/10.1016/j.enconman.2007.12.029.

Pruess, K., 2006. Enhanced geothermal systems (EGS) using CO_2 as working fluid-A novel approach for generating renewable energy with simultaneous sequestration of carbon. Geothermics 35, 351–367. https://doi.org/10.1016/j.geothermics.2006.08.002.

Pruess, K., Oldenburg, C., Moridis, G., 2012. TOUGH2 user's guide, version 2 (revised).

Pruess, K., Spycher, N., 2007. ECO2N – a fluid property module for the TOUGH2 code for studies of CO_2 storage in saline aquifers. Energy Convers. Manag. 48, 1761–1767. https://doi.org/10.1016/j.enconman.2007.01.016.

Randolph, J.B., Adams, B., Kuehn, T.H., Saar, M.O., 2012. Wellbore heat transfer in CO_2-based geothermal systems. Trans. Geoth. Resour. Counc. 36, 549–554.

Randolph, J.B., Saar, M.O., 2011. Combining geothermal energy capture with geologic carbon dioxide sequestration. Geophys. Res. Lett. 38, 1–7. https://doi.org/10.1029/2011GL047265.

Somerton, W.H., 1992. Thermal Properties and Temperature-Related Behavior of Rock/Fluid Systems, 1st ed. Elsevier Science.

Taitel, Y., Bornea, D., Dukler, A.E., 1980. Modelling flow pattern transitions for steady upward gas-liquid flow in vertical tubes. AIChE J. 26, 345–354. https://doi.org/10.1002/aic.690260304.

Turner, R.G., Hubbard, M.G., Dukler, A.E., 1969. Analysis and prediction of minimum flow rate for the continuous removal of liquids from gas wells. J. Pet. Technol. 21, 1475–1482. https://doi.org/10.2118/2198-PA.

Vialle, S., Ajo-Franklin, J., Carey, J.W., 2019. Geological Carbon Storage: Subsurface Seals and Caprock Integrity. American Geophysical Union and John Wiley & Sons, Inc.

Yadigaroglu, G., Hetsroni, G., Hewitt, G.F., 2018. Flow regimes. In: Yadigaroglu, G., Banerjee, S., Hewitt, G.F. (Eds.), Introduction to Multiphase Flow: Basic Concepts, Eds. Applications and Modelling, pp. 95–140. https://doi.org/10.1007/978-3-319-58718-9.

Zhang, L., Cui, G., Zhang, Y., Ren, B., Ren, S., Wang, X., 2016. Influence of pore water on the heat mining performance of supercritical CO_2 injected for geothermal development. J. CO_2 Util. 16, 287–300. https://doi.org/10.1016/j.jcou.2016.08.008.

Zhang, Y., Pan, L., Pruess, K., Finsterle, S., 2011. A time-convolution approach for modeling heat exchange between a wellbore and surrounding formation. Geothermics 40, 261–266. https://doi.org/10.1016/J.GEOTHERMICS.2011.08.003.